AIAA JOURNAL
Vol. 46, No. 8, August 2008

Transverse Injection Through Diamond and Circular Ports into a Mach 5.0 Freestream

Ravichandra Srinivasan* and Rodney D. W. Bowersox†
Texas A&M University, College Station, Texas 77843

DOI: 10.2514/1.29253

Sonic transverse gaseous injection into a Mach 5.0 freestream flow was numerically simulated using two-equation and detached-eddy turbulence models. Circular- and diamond-shaped injectors were investigated in this study. The numerical simulations were compared with available experimental results and it was determined that both the Reynolds-averaged Navier–Stokes and detached-eddy simulation models captured the secondary flow structure. A detailed comparison of the secondary structures was performed for both injectors. Two new vortex structures of practical importance were observed in the diamond-injector flowfield. First, a leading-edge mixing mechanism was identified. Second, a trapped lateral counter-rotating vortex pair was produced. These new structures were observed in both Reynolds-averaged Navier–Stokes and detached-eddy simulation simulations. The detached-eddy simulations indicated that the large-scale structures observed in the plume/wake region of the flowfield were more organized in the diamond-injector test case. To better understand the secondary flow advection mechanism, the magnitudes of the terms in the compressible vorticity transport equation were compared. The diamond-injector structured-grid Reynolds-averaged Navier–Stokes solution was used as a baseline for this study. The inviscid compressibility, vortex-stretching, and baroclinic-torque terms were dominant. Downstream of the barrel-shock region, the baroclinic term was found to diminish when compared with the other inviscid terms. Planar-averaged results for the transport quantities confirmed this behavior. Vortex stretching was found to persist the longest.

Introduction

HYPERSONIC flight within the atmosphere is of current national interest, both military and civilian [1]. Numerous challenges are associated with hypersonic flight. Two important technical challenges that involve the use of jets into a high-speed flow are propulsion and reaction control. The flow structure of perpendicular injection of an underexpanded (the prevalent operating condition for both scramjet and reaction control applications) sonic or supersonic jet into a supersonic freestream has been thoroughly documented [2–4]. In summary, the first flow feature, progressing in the streamwise flow direction, is the interaction or bow shock produced as the freestream impacts the injection stream tube [4]. For injector configurations in which δ/d_{eff} is on the order of one or more, a separation region and a lambda shock form upstream of the injector port [3]. A horseshoe vortex forms between the jet and the interaction shock [2]. After entering the freestream, the underexpanded jet undergoes a rapid Prandtl–Meyer expansion surrounded by a barrel shock. A shock wave normal to the jet path, known as the Mach disk, terminates the barrel shock and compresses the flow to the effective backpressure. Downstream of the Mach disk, a counter-rotating vortex pair forms within the jet plume. Wake vortices are also formed downstream of the injector, between the plume and the floor. The plume vorticity and turbulent mechanisms induce the required large-scale mixing between the jet fluid and the freestream.

The supersonic combustion ramjet (scramjet) is a leading engine candidate for sustained hypersonic flight within the atmosphere [1,5]. Efficient and rapid fuel–air mixing within the scramjet is an important technological challenge [6]. The primary difficulty is the short fuel–air residence time within the engine: typical values are on the order of a few milliseconds. Compounding this challenge is the fact that compressibility slows shear-layer mixing. Turbulence plays an important role in enhancing fuel–air mixing. Hence, characterization of the secondary flow processes is beneficial toward understanding and to improving the mixing processes.

Previous injection studies using experimental methods have been performed to compare the flowfields generated by circular and diamond injectors [7–10]. The mean flow results from these experiments indicate that for a given pressure ratio, the circular injector generates higher peak pressures on the surface. Also, the total pressure losses are higher for circular injectors. The penetration was higher at lower momentum-flux ratios for diamond injectors than with circular and wedge-shaped injectors [7]. Sweeping the diamond injector in the downstream direction was found to increase penetration, similar to the observations made in the case of circular injectors. Wedge-shaped injectors with circular trailing edges have been investigated and the results show that these shapes lead to better performance than with circular injectors [8].

The primary objective of the present study is to characterize and compare the mean shock wave and secondary flow structure for sonic transverse injection of air through diamond and circular orifices into a Mach 5.0 freestream. To this end, numerical simulations with both detached-eddy and Reynolds-averaged closure were performed. The emphasis of the present characterizations is on the shock wave and secondary flow structures. A detailed characterization of the vorticity based on the vorticity transport analysis of the diamond injector is described.

Numerical Methods

Geometry

The domain used in the normal injection simulation was that of the experiments conducted by Bowersox et al. [9]. An illustration of the coordinate system and test section is shown in Fig. 1. Freestream conditions are listed in Table 1. The injector fluid was air in all the test cases. The diamond-injector port had a half-angle of $\gamma = 15$ deg (see Fig. 2). This half-angle was chosen with the goals of 1) a weak leading-edge shock and 2) minimization of tunnel-wall reflections. The injector port had an area of 18.8 mm^2 with an effective diameter of 4.89 mm. The leading edge of the injector was located 71.4 mm downstream of the test-section inlet. The circular injector had the

Received 11 December 2006; revision received 24 May 2007; accepted for publication 18 July 2007.

*Postdoctoral Research Associate, Aerospace Engineering. Member AIAA.
†Associate Professor, Aerospace Engineering. Senior Member AIAA.

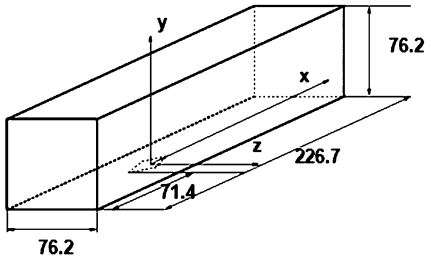

Fig. 1 Coordinate system (in millimeters).

same area as the diamond injector. The centers of the diamond and the circular injectors were aligned. The total pressure of the injectant was 0.10 MPa and the total temperature was 295.0 K. The exit Mach number of the jet was approximately 1.0.

Grid Generation

The flow domain was discretized into a structured grid for the RANS simulation. Flow symmetry was assumed on the x–y plane along the tunnel centerline (see Fig. 3a), based on previous work for a similar configuration [2]. The discretized domain height was limited to $y/d_{\text{eff}} = +7.78$ because the flow structures of interest were within this distance from the tunnel floor. The modeled domain includes the injector port (see Fig. 3b) to include flow losses within the port. The simulation grid was composed of two blocks, one each for the tunnel and the injector, with a total of approximately 5.3×10^6 cells. Grid points were clustered around the injector port and in the plume and wake regions. Clustering was also performed in the boundary layer to ensure that $y^+ < 1$ at the first grid point away from the wall. Grid convergence was performed in situ using the sequencing procedure provided in the flow solver [10]. Convergence studies are described in a later section.

The unstructured-grid growth for the diamond injector is shown in Fig. 4. The initial grid was composed of tetrahedrons. The tetrahedral cells in the boundary layer were converted to prisms to reduce the total cell count. Grids with varying cell counts were generated for both the diamond- and circular-injector configurations. Grids were refined manually as well as using automated techniques. The total number of cells in the grid after refinement was approximately 6.0 million. The cells in the boundary layer were such that $y^+ < 1$ at the first cell off the wall. The height of the computational domain was again restricted to $y/d_{\text{eff}} = +7.78$. The entire lateral width of the experimental domain (i.e., $z/d_{\text{eff}} = +7.78$) was modeled to account for asymmetries in the instantaneous flow.

Boundary Conditions

The freestream Mach number was 5.0 and the inflow boundary was set to match the nozzle exit for the experiments of Bowersox et al. [9]. The boundary-layer thickness was 8.3 mm. Symmetry was specified on the x–y plane along the tunnel centerline for the RANS calculations. Extrapolation conditions were specified on the top and exit surfaces. Adiabatic no-slip conditions were applied at the tunnel floor and injector-port wall. Tangency boundary conditions were applied at the tunnel sidewalls. Mach number, pressure, and density were specified at the injector inlet. The injector-inlet boundary conditions are listed in Table 1. For the turbulence models, the wall boundary conditions recommended by Wilcox [11] were specified. The freestream turbulence-level boundary conditions were varied from 0.5 to 5.0%, as described in the Grid and Solution Convergence section.

Table 1 Freestream and jet conditions

Input	Mach	p_t, MPa	T_t, K	δ, mm
Freestream	5.0	2.4	360	8.3
Jet	1.0	0.1	294	0.0

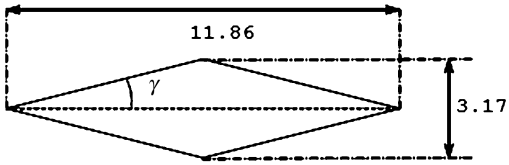

Fig. 2 Diamond-injector geometry (in millimeters).

Simulation Procedure

The Generalized Aerodynamic Simulation Program (GASP) flow solver [10,12] uses structured grids to perform fluid flow simulations. The grid's boundary surfaces were grouped based on boundary conditions discussed in the previous section. The grid was sequenced to obtain solutions on coarse and medium grids. Inviscid fluxes were evaluated using third-order upwinding and Roe's approximate Riemann solver [13] with Harten's entropy correction [14]. The minimum modulus [15] method was used to limit solution variables near discontinuities. Turbulence was simulated using the two-equation k-ω model [16]. Solutions from coarse and medium grids were interpolated to the next-finer sequence by the flow solver to speed up solution convergence and verify grid convergence. Initial iterations on all grid levels were executed with a local Courant–Friedrichs–Lewy (CFL) number. Remaining iterations were executed using the global CFL number.

The Cobalt [17] flow solver was used to simulate the flow using the detached-eddy simulation (DES) turbulence model. Cobalt is a cell-centered unstructured computational fluid dynamics (CFD) code with the ability to solve both Euler and Reynolds-averaged Navier–Stokes (RANS) equations in integral form with second-order accuracy in both space and time. The inviscid fluxes are evaluated using the exact Riemann solver of Gottlieb and Groth [18]. In the present work, the DES version [19] of Menter's shear stress transport (SST) model was used. The simulation was started using the laminar form of the Navier–Stokes equations. The solution was then restarted with Menter's SST turbulence model. After convergence, the solution was again restarted with the DES form of the two-equation model. Initial DES iterations were executed without evaluating any averages to avoid transient flow features. Time-averaging was then enabled and the solution was continued until there was negligible change in averaged results.

Governing Equations and Algorithm for Vorticity Transport Analysis

The vorticity transport analysis was performed on the structured RANS solutions. The reason for this approach is twofold. First, it proved problematic to produce noise-free derivatives on the unstructured grid. Second, the unstructured vorticity analysis indicated that the viscous terms were at least an order of magnitude smaller than the inviscid terms, and both codes produced very similar mean flow structures.

The analysis starts with the vorticity transport equation given by

$$\frac{\mathrm{D}\bar{\omega}}{\mathrm{D}t} = -\bar{\omega}(\nabla \cdot \bar{V}) + (\bar{\omega} \cdot \nabla)\bar{V} - \nabla \times \left(\frac{1}{\rho}\nabla p\right) + \frac{1}{\rho}\nabla \times (\nabla \cdot \bar{\bar{\Pi}}) + \nabla\left(\frac{1}{\rho}\right) \times (\nabla \cdot \bar{\bar{\Pi}}) \tag{1}$$

In the preceding equation, the quantity $\bar{\bar{\Pi}}$ is a second-order tensor. The divergence of this tensor can be evaluated using the following relation.

$$(\nabla \cdot \bar{\bar{\Pi}})_i = \sum_j \frac{\partial \bar{\bar{\Pi}}_{ji}}{\partial x_j} \tag{2}$$

Equation (1) is a vector equation with three components, one each for the x, y, and z components of vorticity. Assuming steady-state conditions, the full form of the x vorticity transport equation is

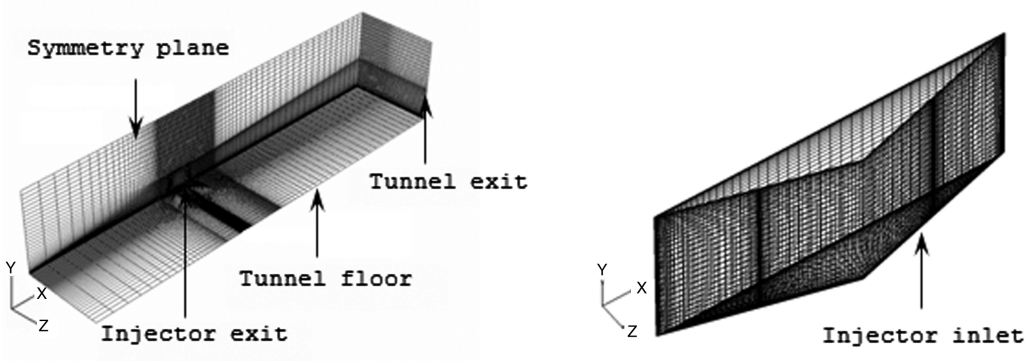

a) Full grid used in RANS simulation b) Injector grid

Fig. 3 Structured grids for RANS simulations.

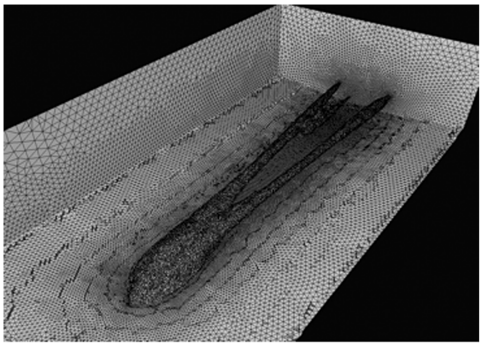

Fig. 4 Unstructured-grid generation for DES simulations showing clustering around the injector exit and in the wake/plume region downstream of the injector.

$$\bar{V}_x\frac{\partial\bar{\omega}_x}{\partial x}+\bar{V}_y\frac{\partial\bar{\omega}_x}{\partial y}+\bar{V}_z\frac{\partial\bar{\omega}_x}{\partial z}=-\bar{\omega}_x\frac{\partial\bar{V}_x}{\partial x}-\bar{\omega}_x\frac{\partial\bar{V}_y}{\partial y}-\bar{\omega}_x\frac{\partial\bar{V}_z}{\partial z}+\bar{\omega}_x\frac{\partial\bar{V}_x}{\partial x}+\bar{\omega}_y\frac{\partial\bar{V}_x}{\partial y}+\bar{\omega}_z\frac{\partial\bar{V}_x}{\partial z}+\frac{1}{\rho^2}\left[\frac{\partial\rho}{\partial y}\frac{\partial p}{\partial z}-\frac{\partial\rho}{\partial z}\frac{\partial p}{\partial y}\right]+\frac{1}{\rho}\left[\frac{\partial T_3^L}{\partial y}-\frac{\partial T_2^L}{\partial z}\right]+\frac{1}{\rho}\left[\frac{\partial T_3^T}{\partial y}-\frac{\partial T_2^T}{\partial z}\right]-\frac{1}{\rho^2}\left[T_3^L\frac{\partial\rho}{\partial y}-T_2^L\frac{\partial\rho}{\partial z}\right]-\frac{1}{\rho^2}\left[T_3^T\frac{\partial\rho}{\partial y}-T_2^T\frac{\partial\rho}{\partial z}\right] \quad (3)$$

The y and z vorticity relations are similar to the preceding x vorticity. The quantities denoted by T_i^L and T_i^T are obtained using the following relations.

$$T_1^L=\frac{\partial\bar{\bar{\Pi}}_{xx}^L}{\partial x}+\frac{\partial\bar{\bar{\Pi}}_{yx}^L}{\partial y}+\frac{\partial\bar{\bar{\Pi}}_{zx}^L}{\partial z}$$

$$T_1^T=\frac{\partial\bar{\bar{\Pi}}_{xx}^T}{\partial x}+\frac{\partial\bar{\bar{\Pi}}_{yx}^T}{\partial y}+\frac{\partial\bar{\bar{\Pi}}_{zx}^T}{\partial z}$$

where

$$\bar{\bar{\Pi}}=\Pi_{ij}^L+\Pi_{ij}^T$$

$$\Pi_{ij}^L=\mu\left(\frac{\partial u_i}{\partial x_j}+\frac{\partial u_j}{\partial x_i}\right)+\lambda\delta_{ij}\nabla.\mathbf{V}$$

$$\Pi_{ij}^T=2\mu_T\left(S_{ij}-\frac{1}{3}\frac{\partial\bar{u}_k}{\partial x_k}\delta_{ij}\right)-\frac{2}{3}\bar{\rho}k\delta_{ij}$$

$$S_{ij}=\frac{1}{2}\left(\frac{\partial u_i}{\partial x_j}+\frac{\partial u_j}{\partial x_i}\right)$$

The x component of the stress terms are given by the following relations. The y and z terms can be obtained similarly.

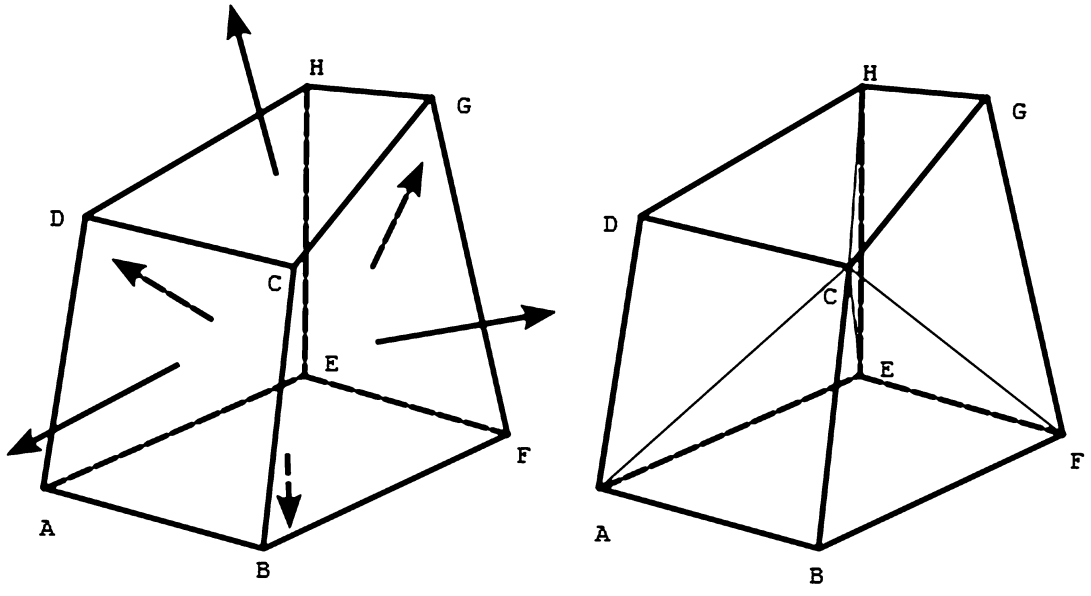

Fig. 5 Surface area and volume calculation for a hexahedral cell.

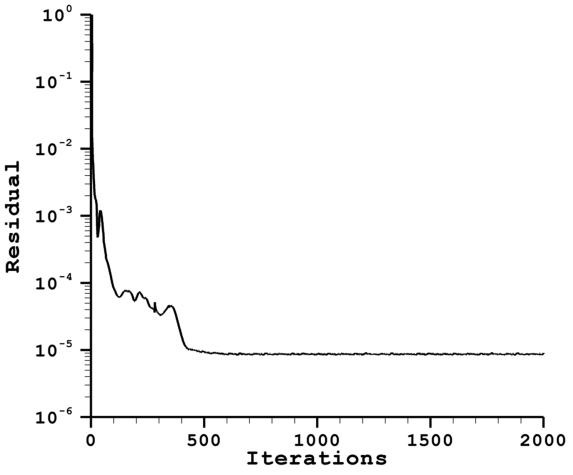

a) Residual for fine grid

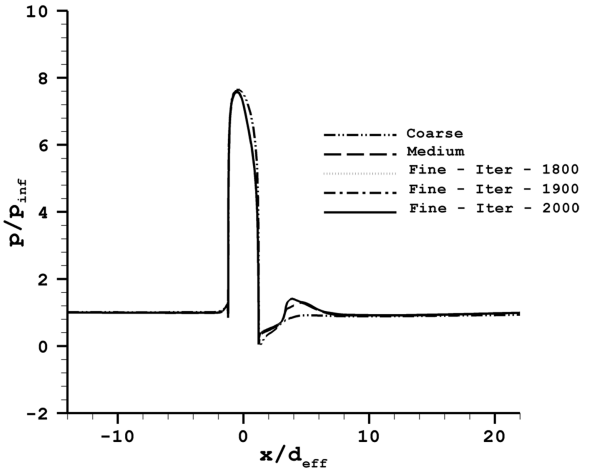

b) Pressure along axial centerline of the tunnel floor

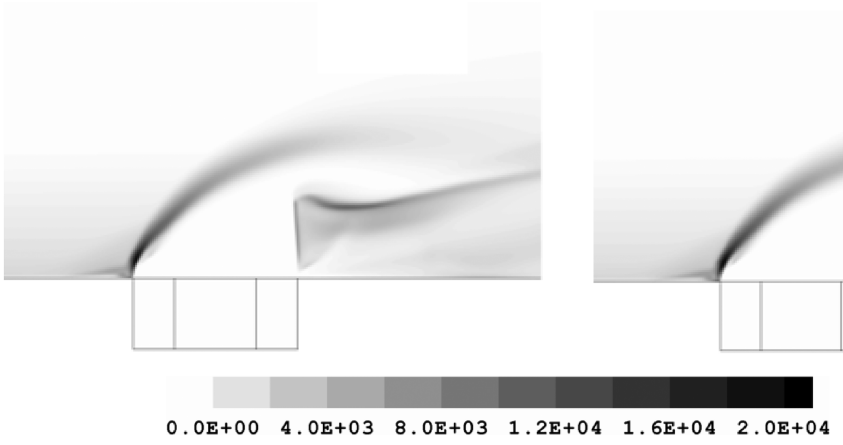

c) Turbulent kinetic energy: 5%

d) Turbulent kinetic energy: 0.5%

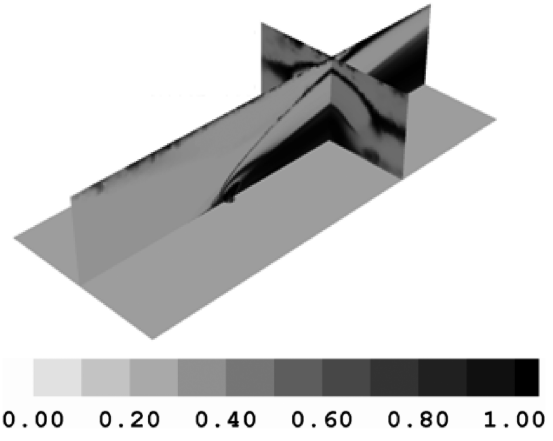

e) Ratio of resolved turbulent kinetic energy to total kinetic energy for DES model

Fig. 6 Simulation uncertainties.

$$\Pi_{xx} = 2\mu\frac{\partial u}{\partial x} + \lambda\frac{\partial u_i}{\partial x_i} + 2\mu_T\left(\frac{\partial u}{\partial x} - \frac{1}{3}\frac{\partial u_i}{\partial x_i}\right) - \frac{2}{3}\bar{\rho}k$$

$$\Pi_{xy} = \Pi_{yx} = \left(\frac{\partial u}{\partial y} + \frac{\partial v}{\partial x}\right)(\mu + \mu_T)$$

Table 2 DES simulation details

Model	Iterations	Time step
Laminar	1000	CFL
SST: RANS	2000	CFL
SST: DES, transient	3000	1e − 6
SST: DES, averaged	6000	1e − 6

The terms in Eq. (3) and the corresponding y and z equations were evaluated using an in-house code. The inputs for the program were the grid file and steady-state RANS solution. The following variables are used in the program: density, velocity components, pressure, and Reynolds stress tensor components. Solution results were stored at grid points within the domain. Time-averaged temperature was calculated using the ideal-gas relation and dynamic viscosity was calculated using Sutherland's law.

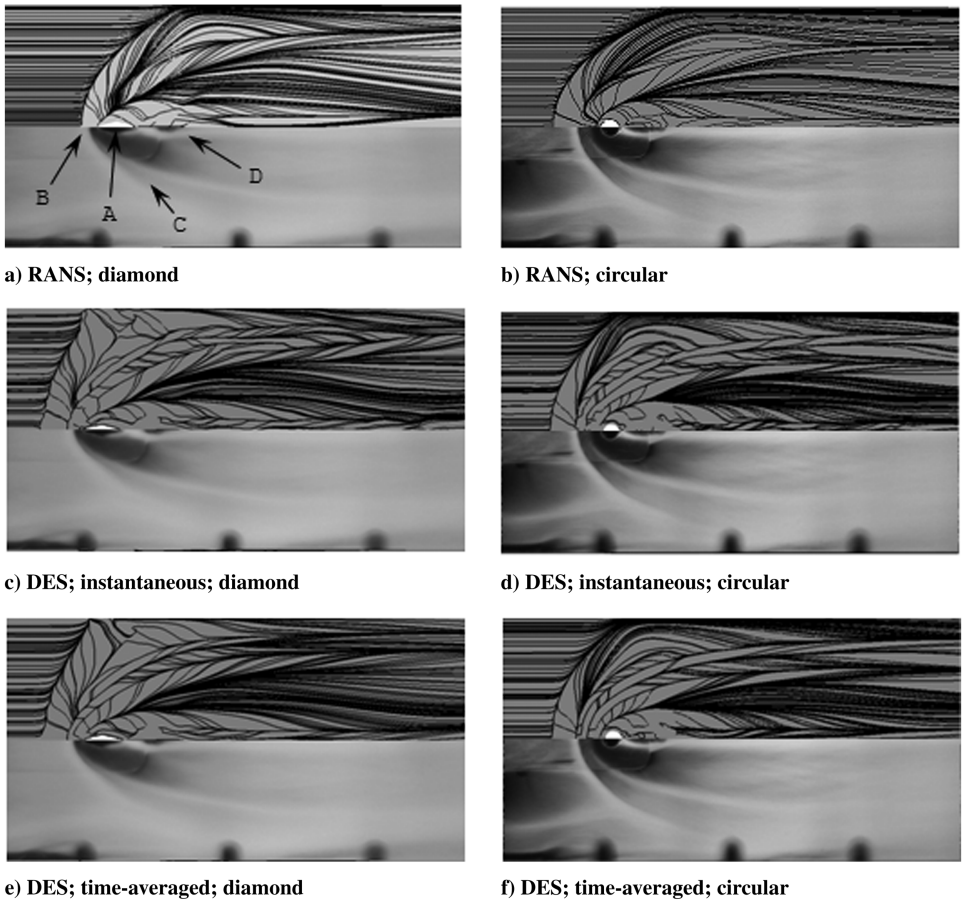

a) RANS; diamond b) RANS; circular

c) DES; instantaneous; diamond d) DES; instantaneous; circular

e) DES; time-averaged; diamond f) DES; time-averaged; circular

Fig. 7 Surface oil-flow comparison: numerical result (each top half) and experimental data (each bottom half): a) injector, b) shock-induced separation, c) horseshoe vortex, and d) wake vortex.

The nodal coordinates of the grid and also the average data for each cell in the domain were read in from the structured-grid RANS results. Using the nodal coordinates, the normal vectors of the cell faces were evaluated, along with cell face areas and cell volumes. The gradient theorem was then used to form the necessary derivatives of the variables. These derivatives were then used in calculating the terms in the vorticity transport equation. The surface area of a cell face was evaluated using the following relation (see Fig. 5a for the node references).

$$\mathbf{S}_{ABCD} = \tfrac{1}{2}(\mathbf{r}_{AC} \times \mathbf{r}_{BD}) \tag{4}$$

Each hexahedron in the structured grid was divided into three pyramids, as shown in Fig. 5b. The total volume of the hexahedron is the sum of the volumes of these pyramids [Eqs. (5) and (6)].

$$\mathcal{V}_{CBFEA} = \tfrac{1}{24}(\mathbf{r}_{CB} + \mathbf{r}_{CF} + \mathbf{r}_{CE} + \mathbf{r}_{CA}) \cdot (\mathbf{r}_{BE} \times \mathbf{r}_{FA}) \tag{5}$$

$$\mathcal{V}_{\text{hex}} = \mathcal{V}_{CBFEA} + \mathcal{V}_{CFGHE} + \mathcal{V}_{CAEHD} \tag{6}$$

Table 3 Flow-structure location predicted by RANS and DES

Injector	Structure	Experiment	RANS: structured grid	DES: unstructured grid
Diamond	LE separation [a]	0.0080	0.0053	0.0128
	TE merging [b]	0.0181	0.0192	0.0203
	HS separation [c]	0.0340	0.0405	0.0407
Circular	LE separation [a]	0.0108	0.0122	0.0162
	TE merging [b]	0.0150	0.0181	0.0189
	HS separation [c]	0.0387	0.0304	0.0322

[a]Leading-edge separation measured from the injector leading edge.
[b]Trailing-edge merging of wake vortex measured from the injector trailing edge.
[c]Horseshoe-vortex separation at the injector trailing edge.

The gradient theorem used to evaluate the required derivatives is given by

$$\frac{1}{\mathcal{V}} \iiint_{\mathcal{V}} \nabla\phi \, \mathrm{d}\mathcal{V} = \frac{1}{\mathcal{V}} \oiint_{\mathcal{A}} \phi \hat{n} \, \mathrm{d}\mathcal{A} \tag{7}$$

For example, the x derivative of the variable ϕ is given by

$$\frac{1}{\mathcal{V}} \iiint_{\mathcal{V}} \frac{\partial\phi}{\partial x} \, \mathrm{d}\mathcal{V} = \frac{1}{\mathcal{V}} \oiint \phi \hat{n}_x \, \mathrm{d}\mathcal{A} \tag{8}$$

The right-hand side of the preceding equation is evaluated as

$$\begin{aligned} \frac{\partial\phi}{\partial x} = \frac{1}{\mathcal{V}} \iiint_{\mathcal{V}} \frac{\partial\phi}{\partial x} \, \mathrm{d}\mathcal{V} = \Bigg[& \frac{(\phi_{i-1} + \phi_i)}{2} n_{x_{i-\frac{1}{2}}} \mathcal{A}_{i-\frac{1}{2}} \\ & + \frac{(\phi_i + \phi_{i+1})}{2} n_{x_{i+\frac{1}{2}}} \mathcal{A}_{i+\frac{1}{2}} \frac{(\phi_{j-1} + \phi_j)}{2} n_{x_{j-\frac{1}{2}}} \mathcal{A}_{j-\frac{1}{2}} \\ & + \frac{(\phi_j + \phi_{j+1})}{2} n_{x_{j-\frac{1}{2}}} \mathcal{A}_{j+\frac{1}{2}} \frac{(\phi_{k-1} + \phi_k)}{2} n_{x_{k-\frac{1}{2}}} \mathcal{A}_{k-\frac{1}{2}} \\ & + \frac{(\phi_k + \phi_{k+1})}{2} n_{x_{k-\frac{1}{2}}} \mathcal{A}_{k+\frac{1}{2}} \Bigg] \Big/ \mathcal{V} \end{aligned} \tag{9}$$

The cell average values of the y and z derivatives are evaluated in a similar fashion.

Numerical Convergence and Validation

Grid and Solution Convergence

For all the simulations presented here, the residual (L_2 norm) was reduced by at least five orders of magnitude. A plot of the residual for iterations on the fine grid is shown in Fig. 6a. It was observed that there was no change in the residual value after about 500 iterations.

The grid-sequencing option in GASP was used to ensure that the solution obtained was grid-converged. From the initial (fine) grid input into GASP, two additional grid levels were generated. The medium grid was obtained by eliminating every second point in the fine grid, and the coarse grid was obtained by eliminating every second point in the medium grid. Solutions were then generated for the coarse, medium, and fine grids. A plot of pressure along the centerline of the tunnel floor is shown for the three grid levels in

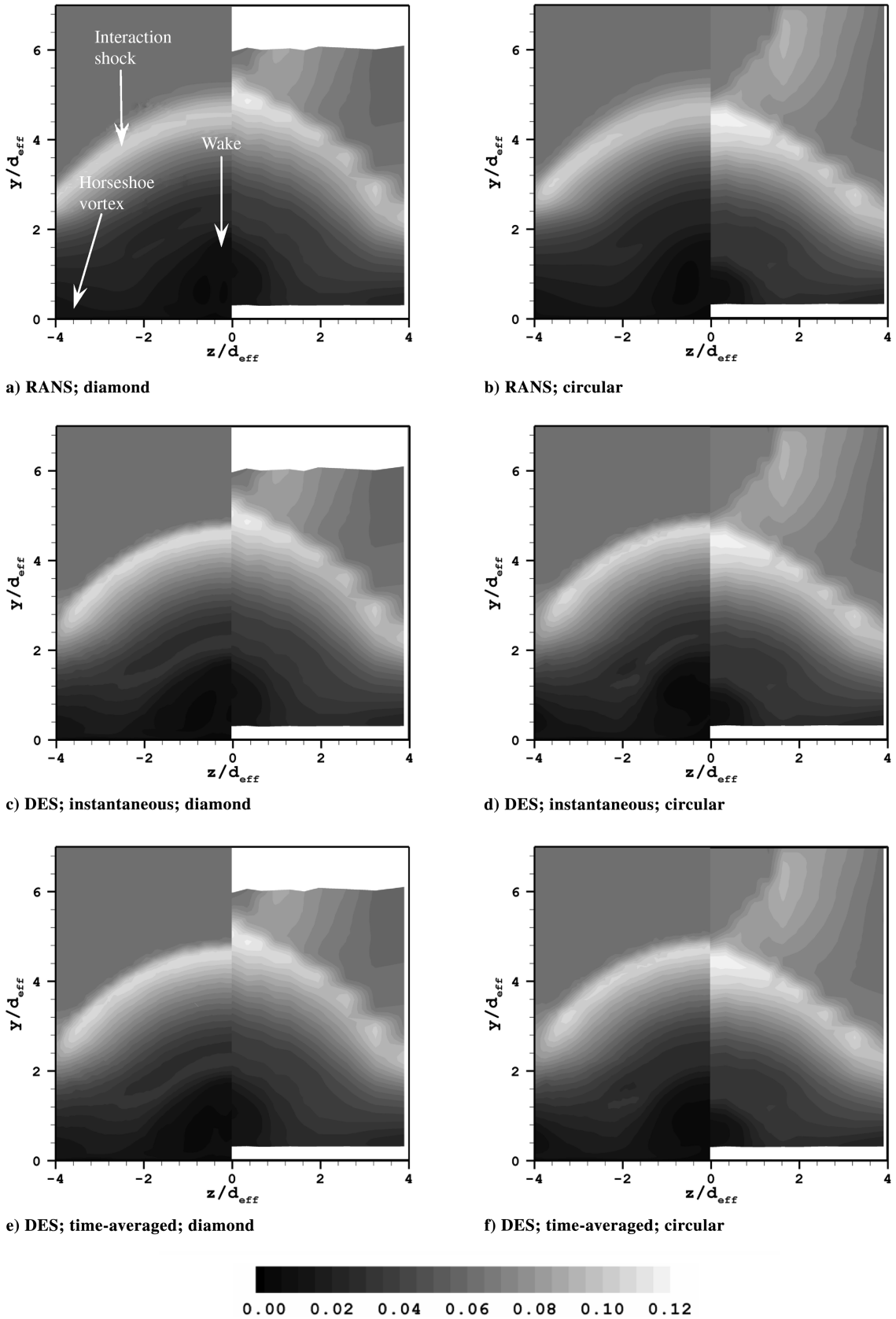

a) RANS; diamond

b) RANS; circular

c) DES; instantaneous; diamond

d) DES; instantaneous; circular

e) DES; time-averaged; diamond

f) DES; time-averaged; circular

Fig. 8 Diamond- and circular-injector stagnation pressure ratio p_{02}/p_0 contours at location $x/d_{\text{eff}} = +8.0$: numerical result (each left half) and experimental data (each right half).

Fig. 6b. The pressure plots for the medium and fine grids coincide, indicating that grid convergence was achieved. The secondary flow structures found in the fine grid were also observed in the medium grid.

Grid convergence studies were conducted for the Cobalt solutions using multiple grids of 4.5 and 6.0 million cells. Time-step convergence was conducted using two different time steps of $1E-6$ and $2E-6$ s. The maximum variation in the turbulent statistics was less than 3.0% for all grids and time steps tested. For the present study, the fine grid and smallest time step were used. Table 2 lists details of the calculation, including iterations, models, and time steps. As indicated in the Boundary Conditions section, two freestream turbulence-level boundary conditions were examined. The resulting turbulent kinetic energy distributions are shown in Figs. 6c and 6d. The results imply that the results in the plume region were insensitive to this boundary condition over the range tested (0.5–5.0%). As a measure of the detached-eddy turbulence resolution, a contour plot of the ratio of resolved turbulent kinetic energy to the total kinetic energy is shown in Fig. 6e. This plot indicates that a significant portion (greater than 90%) of the kinetic energy in the region around the injector and the plume was resolved.

The compressible vorticity transport equation was solved with the structured-grid RANS solution as the initial condition. The RANS solution was obtained using a third-order-accurate scheme. The primary area of interest was the region surrounding the injector orifice. The grid in this region was mostly uniform, with stretching in the y direction. Based on this information and the fact that a second-order technique was used in evaluating the terms in the vorticity transport equation, the order of accuracy for the vorticity transport equation was deemed to be $\mathcal{O}(\Delta x)$.

Comparison with Experimental Data

Numerical and experimental [9] surface oil-flow visualizations for case 1 (Table 1) are shown in Fig. 7. The experimental result is annotated, indicating the salient flow features. The freestream flow is from left to right. The first feature observed in the flow direction is the shock-induced separation. This region is difficult to discern in the grayscale experimental image. The separation is similar to that seen in results obtained from the GASP simulation. The instantaneous and time-averaged DES results predict a larger separation region. The horseshoe vortex wraps around the injector and can be observed in the images from both RANS and DES results. The distance separating the two arms of the vortex is correctly predicted. At the trailing edge of the injector port, a pair of wake vortices is clearly seen in experimental results. Although not clearly visible in numerical oil-flow results, the presence of these wake vortices can be observed in the streamlines, as presented later in the discussion on the flow structures. In summary, the predicted size and location of the upstream-surface oil-flow features were better for the RANS results, whereas the DES overpredicts the separation. Downstream-flow feature-location predictions are favorable for both RANS and DES. The locations of features are listed in Table 3.

A comparison of pitot pressure obtained from RANS simulations and experiments is shown in Fig. 8. The plane of data shown is at a distance of $x/d_{\text{eff}} = +8.0$. The extent of the data shown in the y and z

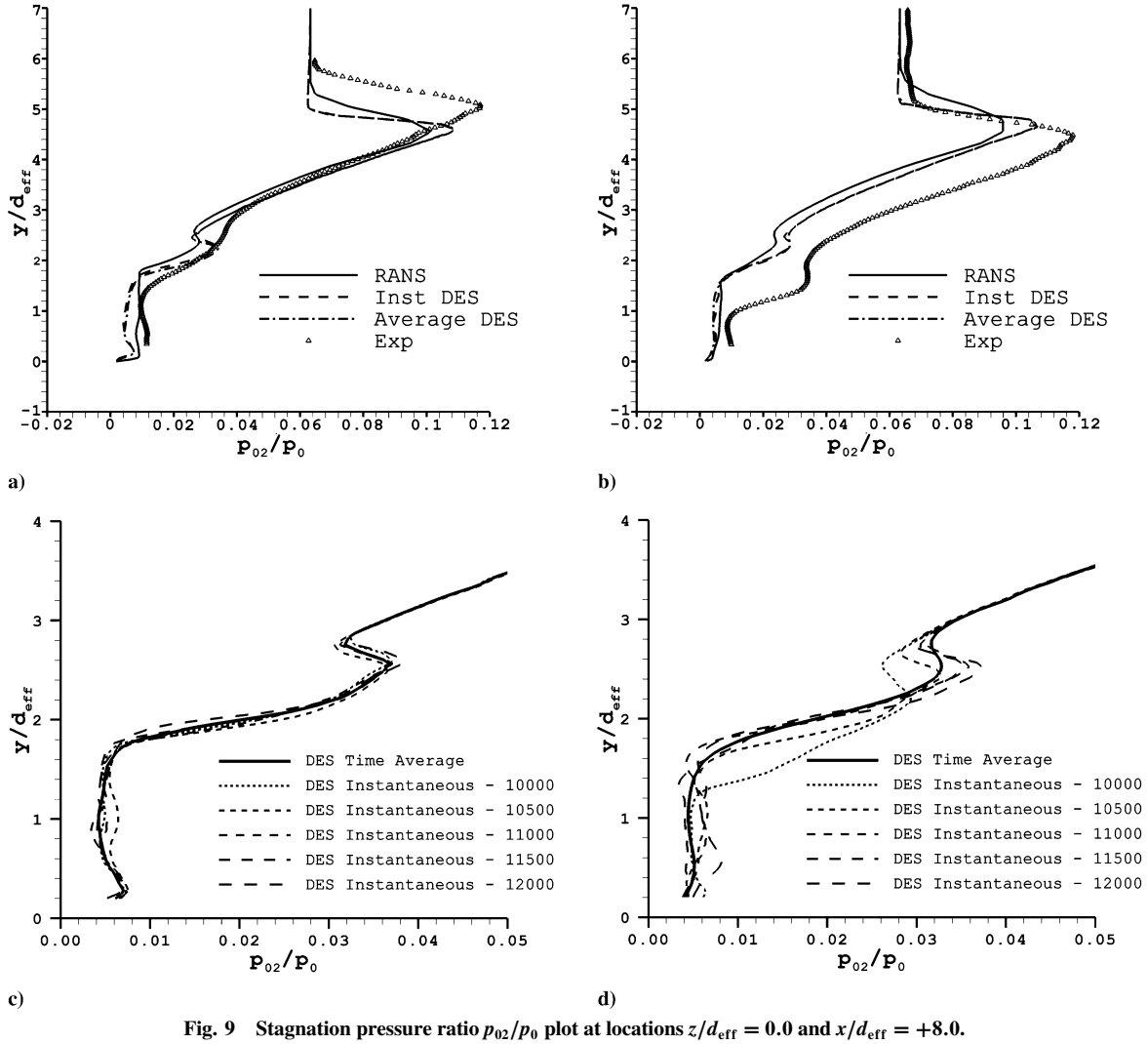

Fig. 9 Stagnation pressure ratio p_{02}/p_0 plot at locations $z/d_{\text{eff}} = 0.0$ and $x/d_{\text{eff}} = +8.0$.

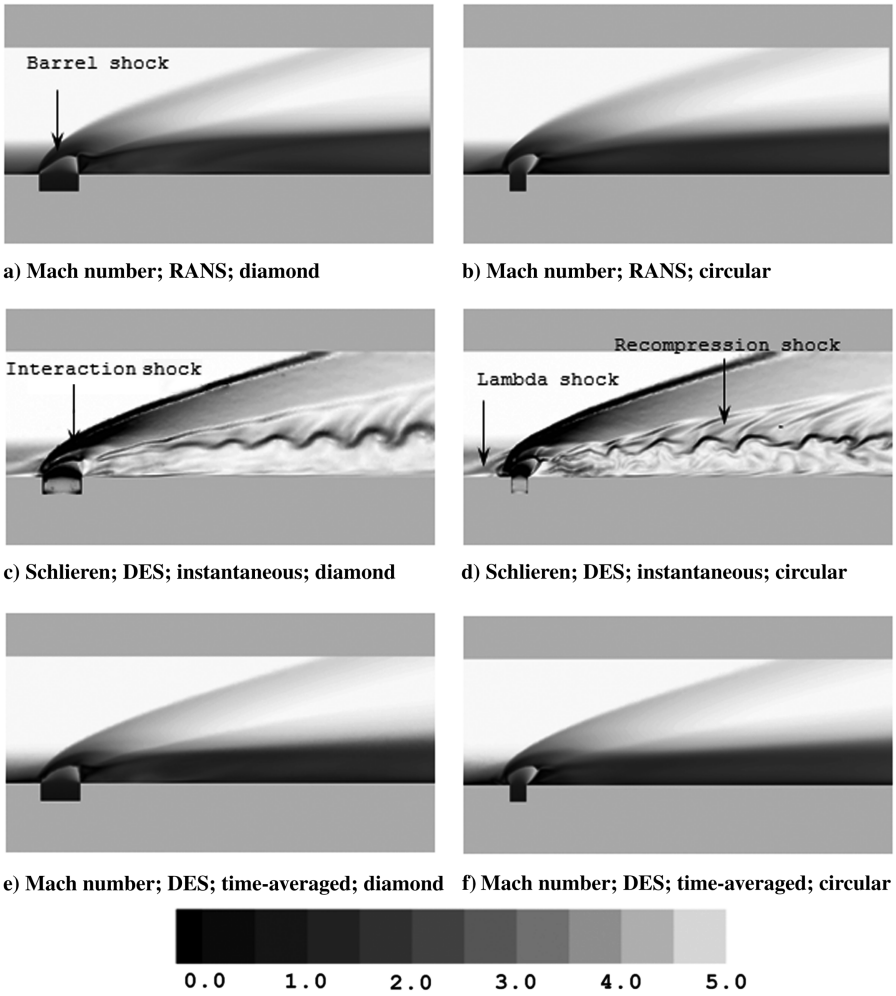

a) Mach number; RANS; diamond

b) Mach number; RANS; circular

c) Schlieren; DES; instantaneous; diamond

d) Schlieren; DES; instantaneous; circular

e) Mach number; DES; time-averaged; diamond

f) Mach number; DES; time-averaged; circular

Fig. 10 Mach number plots along the tunnel center plane for the RANS and time-averaged DES results; a scale is shown for the Mach number.

directions is 0.0 to 7.0 and −4.0 to 4.0, respectively. The freestream flow is directed into the page. The numerical results are shown on the left and the experimental data are shown on the right for better comparison. It should be noted that experimental data are not available below $y/d_{\text{eff}} = 0.3$.

The wake and plume are represented by the bell-shaped structure centered around $z/d_{\text{eff}} = 0.0$ below $y/d_{\text{eff}} = 3.0$. The inner part of this region is characterized by low total pressures (p_{02}/p_0 of approximately 0.01–0.03). The width of wake region is maximum at the floor and extends about $2.0^* d_{\text{eff}}$ on either side of the centerline.

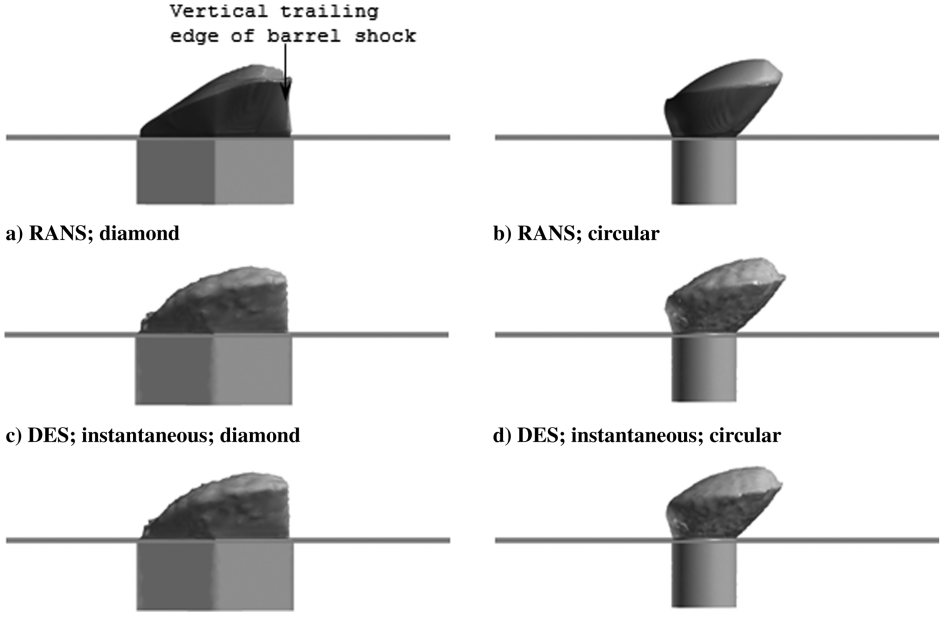

a) RANS; diamond

b) RANS; circular

c) DES; instantaneous; diamond

d) DES; instantaneous; circular

e) DES; time-averaged; diamond

f) DES; time-averaged; circular

Fig. 11 Barrel-shock surface for diamond and circular injectors; view is from the positive z axis; freestream flow is from left to right.

The height of the wake region is approximately $1.8^{*}d_{\text{eff}}$. It is observed that the boundary layer is thinner on either side of the wake region, due to the upwash created by the counter-rotating vortex pair. By comparing the CFD results with experimentally measured pitot pressure, it was found that the pressure of the wake region was overpredicted by approximately 20–30%. This indicates that the high-momentum freestream flow diffuses more into the plume/wake region in the experiment. The plume/wake extends to the same height in the CFD results as it does in experiments. The DES results appear marginally better than RANS because there is higher diffusion around the outer boundary of the plume/wake region. Boundary-layer thinning around the plume/wake is observed in experimental and numerical results. A portion of the horseshoe vortex can be seen at the outer edges of the image, near the floor.

Above the wake region is where the jet plume and freestream fluid interact, forming a shear layer. The numerical prediction of the shear-layer height matches the experimental value of $3.0^{*}y/d_{\text{eff}}$. Beyond this shear layer is the inviscid region. The interaction shock wave is the last significant feature observed in the plots. It is represented by the arch extending across the entire measurement plane with the peak located at $y/d_{\text{eff}} = 5.0$ and centered around $z/d_{\text{eff}} = 0.0$. Moving along the positive and negative z-axis direction, the height of the shock wave decreases and at $z/d_{\text{eff}} = \pm 4.0$ it is $y/d_{\text{eff}} = 3.0$. The shock location was accurately predicted, when compared with experimental results. Overall, the pitot-pressure structure of the flowfield was captured by the simulations. However, in the periphery of the plume/wake region, the values are higher in the CFD, particularly RANS results.

A line plot of the pitot pressure along $z/d_{\text{eff}} = 0.0$ for both experimental and numerical data is shown in Fig. 9. Overall, the agreement between the computation and experiment was considered good, with the largest differences occurring near the interaction shock and within the plume/wake region. The vertical extent of the shock was underpredicted by 10%, which corresponds to about 3.0 mm, or one probe diameter. The pitot-pressure magnitude near the shock was underpredicted by about 20%. Assuming a conical shock wave, the observed difference corresponds to a local flow-angle difference of approximately 2 deg, which indicates that the flow is sensitive to small errors in this region. In the wake and the plume regions, the predicted values follow the trend of the experimental results.

The line plot for the circular injector indicates that the salient flow structures are captured. However, the noticeable difference in the experimental and numerical results is a steady offset that is on the order of the diameter (3 mm) of the probe used in the experiments. The apparent discrepancy between the experimental and CFD results in the plume/wake region appears to not be systematic. The differences are about the same. However, the trends appear to be reversed. At this point, there is not sufficient information to discern the exact cause for the differences. One possible reason could be errors in the pitot pressure due to large flow angles in this region (up to 20 deg relative to the x axis). The instantaneous variation of the flow can be seen in Figs. 9c and 9d for diamond- and circular-injector DES simulations. Other sources could be related to the turbulence-model performance in the presence of strong secondary motions [16]. In any event, the qualitative structure is captured and, for the most part, the quantitative results were deemed acceptable for the present purpose of flow-structure characterization and comparison.

The ripples observed in the experimental shock structure are artifacts produced during the pitot-pressure measurement. A five-hole probe was used in the experiments to measure the total and the static pressures. These values were then used to obtain the flow Mach

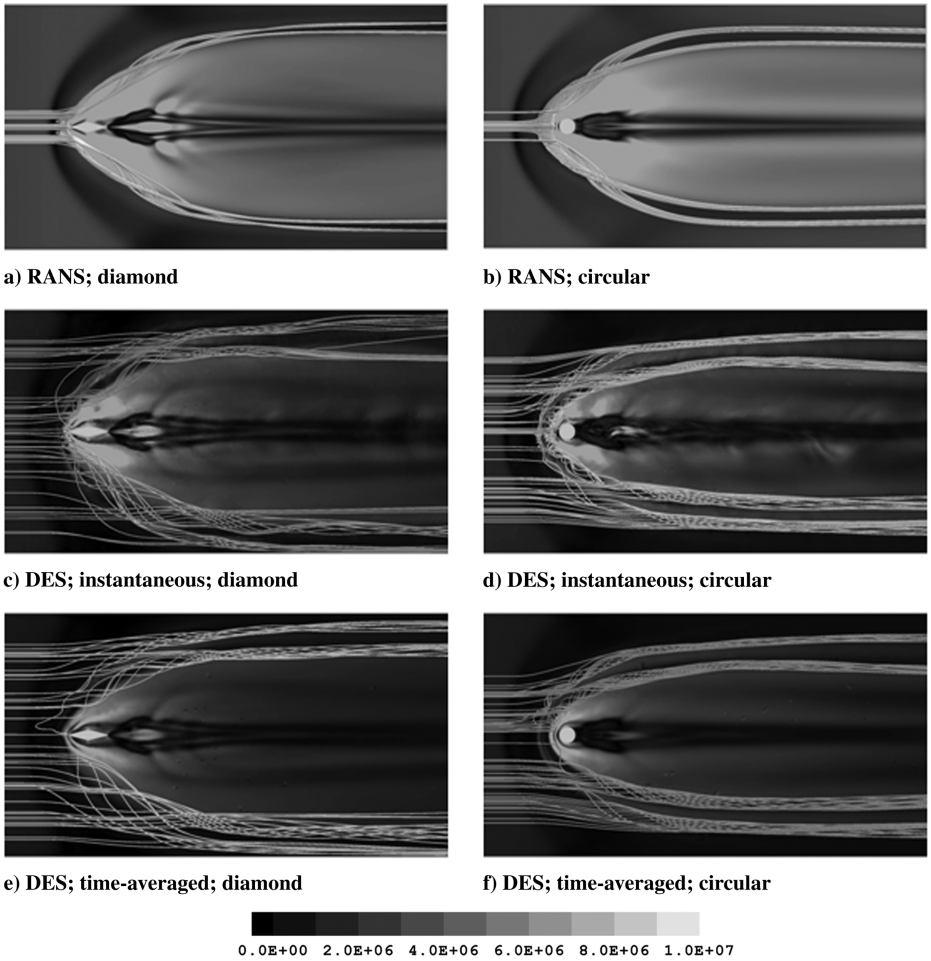

Fig. 12 Top view of streamlines showing the horseshoe-vortex structures for diamond and circular injectors; tunnel surface has contours of vorticity magnitude.

number. The data were obtained along lines that were separated by 1/16th of an inch in the z direction. This leads to the formation of the ripple artifacts in the plots of experimental data and the CFD simulation is not expected to capture this phenomenon. The resolution in the y direction is much higher, because the probe traverses in a continuous fashion.

Results and Discussion

Shock Structures

The flow structure generated by transverse injection into a supersonic flow is dominated by primary and secondary shocks. In the subsequent discussion, the shock structures due to the diamond injector are described and the differences with the more canonical circular injector are highlighted.

Interaction and Recompression Shocks

Plots of Mach number and numerical schlieren on the tunnel centerline plane are shown in Figs. 10a–10f. Mach number was chosen for the RANS and time-averaged DES results and schlieren was chosen for the instantaneous results to clearly show the resolved flow structures. Comparing the interaction shocks for the diamond (left image) and circular (right image) injectors in Figs. 10c and 10d, it was concluded that the shock structures were similar along the centerline. Focusing on the diamond-injector shocks, the shock surface starts just upstream of the injector orifice. The angle of the shock surface along this plane decreases with increasing distance from the tunnel floor, due to the effect of lower Mach numbers in the incoming freestream boundary layer. The location and shape of the interaction shock is identical in RANS and DES results.

The lambda shock is apparent in schlieren images presented in Figs. 10c and 10d. The lambda shock extended further upstream for the circular injector. This was expected, because the circular injector generates a larger recirculation zone upstream of the injector, as seen in the surface oil-flow visualizations.

The recompression shock is created when the freestream flow passes through the interaction shock and interacts with the jet plume that is turning in the freestream direction. The recompression shocks were also very similar for the two injectors. The origin of the recompression shock is located just downstream of the injector exit, at $y/d_{\text{eff}} = 1.6$ from the tunnel floor. Pressure rise across the recompression shock is approximately $0.2^{*}p/p_{\text{inf}}$, which is about 10% of the pressure increase across the interaction shock. Unlike the interaction shock, which appears to be the same in the instantaneous and time-averaged DES, the recompression shock is unsteady. The shock is formed by the coalescence of waves generated due to the unsteady flow structures in the plume and the supersonic freestream.

Barrel Shock

An isosurface representation of the barrel-shock structure is shown in Fig. 11 for the diamond and circular injectors. The diamond-injector barrel shock starts as a point at the tip of the injector exit upstream of the origin, which is clearly shown on the isosurface. The leeward surface of the barrel shock resembles a V. The fan angle and inclination of this surface are favorable for the formation of interesting vortex structures (discussed in a later section). The barrel shock also exhibits axis switching [7]; that is, it expands more in the

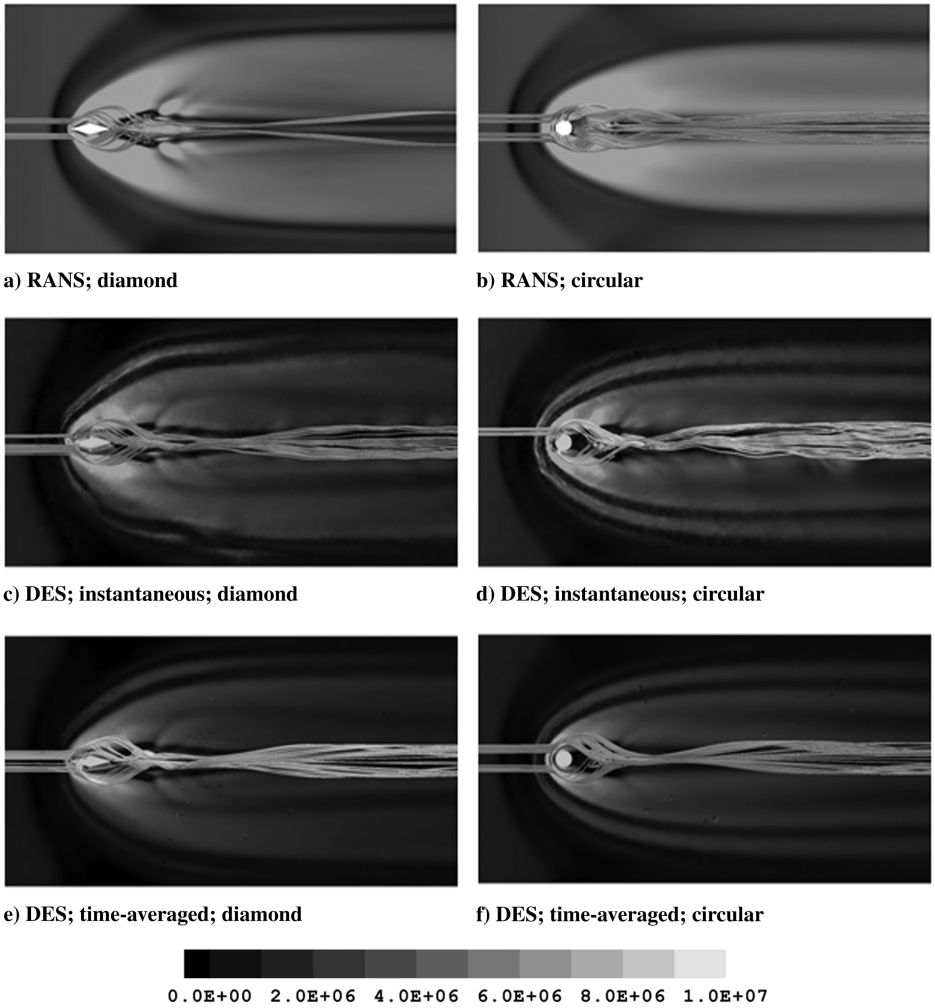

Fig. 13 Top view of streamlines showing the wake vortex structures for diamond and circular injectors; tunnel surface has contours of vorticity magnitude.

lateral direction than in the freestream direction. This behavior is also observed in transverse injection with elliptic ports [20].

The shape of the barrel shock generated by circular injectors is more conventional and resembles a barrel tilted in the downstream direction. The Mach disk is more prominent in this shock than with that produced by diamond-shaped injectors. There is no perceptible change in the overall shape of the instantaneous shape of the barrel shock when compared with the RANS and time-averaged DES results. This is an important observation, because the shape of the shock affects the secondary flow structures in the vicinity of the injector orifice.

Vortex Structures

Horseshoe Vortex

The high pressure due to the interaction shock causes the incoming boundary layer to separate. The prevalent negative z vorticity leads to the formation of the horseshoe vortex (shown in Fig. 12). Moving away from the tunnel centerline toward the sidewalls, it was found that the horseshoe vortex wraps around the injector exit. The negative z vorticity is changed to negative x vorticity on the positive z-axis side and positive x vorticity on the negative z-axis side. The core of the horseshoe vortex is composed of fluid from the inner region of the boundary layer. Additional freestream boundary-layer fluid is trapped by this vortex as it wraps around the injector exit.

The DES results show multiple horseshoe vortices compared with the RANS results. A larger separation region was predicted by the DES around the upstream edge of the injector leading to the development of multiple horseshoe vortices, which was observed for both diamond and circular injectors. The RANS result on the unstructured grid was generated and analyzed, which confirmed that this behavior was due to the DES model.

Wake Vortex Pair

A pair of vortices form on both sides of the tunnel centerline near the injector trailing edge, as shown in Fig. 13. Fluid from the outer regions of the freestream boundary layer (around the tunnel centerline) moves over the horseshoe vortex and down into the region on either side of the injector port, due to the lower static pressure in the region downstream of the barrel shock. The flow sweeping into this region from either side interacts and gives rise to the wake vortex pair.

For the diamond injectors, the wake vortices form a coherent pair around $x/d_{\text{eff}} = 3.0$. Immediately downstream of this location, the wake vortices start to lift off of the tunnel floor, due to the action of the counter-rotating vortex pair (CVP). Further downstream, it was found that the wake vortex merges with the CVP (described in the next section). The increase in lateral separation between the vortices and their curvature indicates that the merging process is completed close to the end of the domain (i.e., after $x/d_{\text{eff}} = 20.0$).

In the case of circular injectors, the wake vortices form nodes close to the floor at location $x/d_{\text{eff}} \approx 3.0$ downstream of the injector. The fluid traveling upstream of the nodes is fed into the CVP, and the fluid traveling downstream stays close to the floor without interacting with the CVP.

Leading-Edge Mixing Vortex

A pair of vortices is formed at the leading edge of the diamond-injector exit, as shown in Fig. 14. The shear on the injector exit plane

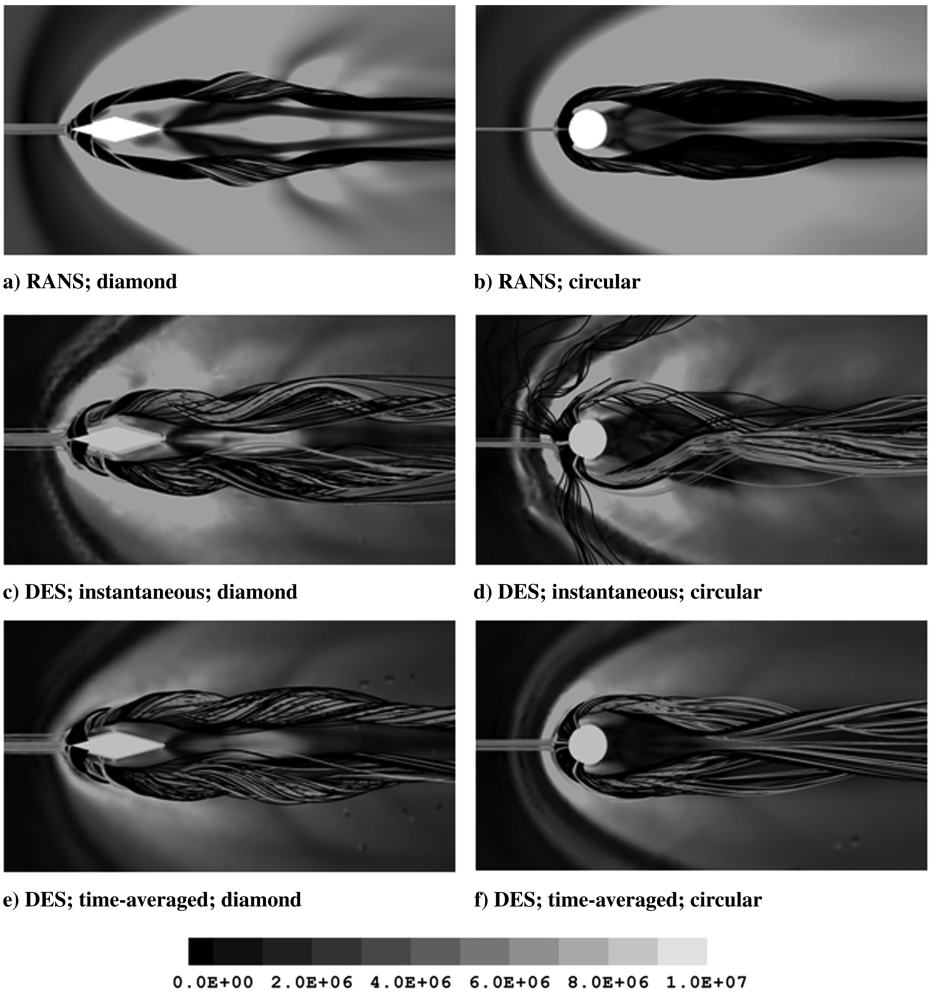

Fig. 14 Top view of the streamlines showing the leading-edge mixing vortex for diamond and circular injectors: flow from the freestream (gray streamlines) and flow from the injector (black streamlines); tunnel surface has contours of vorticity magnitude.

due to the action of the freestream fluid and the injectant, along with corner vorticity in the diamond-injector port, leads this vortex pair. The two vortices undergo lateral separation as the fluid travels downstream, caused by the expansion of the injector fluid in the lateral direction due to axis-switching. The maximum separation between the vortices occurs close to the trailing edge of the injector port and is approximately $2.0^* d_{\text{eff}}$. It is observed that this vortex pair entrains fluid from the outer regions of the freestream boundary layer, as well as from the injector. Thus, this vortex pair could induce enhanced mixing of freestream and injector fluids. The circular-injector geometry produces a somewhat similar structure. This vortex is a single structure and is similar to the horseshoe vortex. The vortex core is on a constant-y plane at about $0.2^* d_{\text{eff}}$ from the tunnel floor. In both cases, this vortex structure eventually feeds into the CVP.

Lateral Counter-Rotating Vortex Pair

A new vortex pair has been identified in the diamond-injector flowfield [21]. This new pair is located just downstream of the barrel shock and the axes are oriented in the z-axis direction. The streamlines representing this vortex pair are shown in Fig. 15. This new structure is particularly interesting because it has the potential to serve as a gas-dynamically induced flame holder. It was observed that this structure is present in the RANS and in the instantaneous and time-averaged DES results.

After analyzing the flow structures in detail, it was found that the lateral counter-rotating-vortex (LCVP) formation is closely coupled to the barrel-shock shape. The barrel-shock shape is described in an earlier section. This shock shape for the diamond-injector facilitates the formation of the LCVP. The low pressures generated on the downstream side of the barrel shock cause part of the incoming freestream boundary-layer fluid to move up from the tunnel floor. This fluid interacts with the injector fluid that is passing through the barrel shock and turning in the freestream direction. A recirculation region is set in motion due to this interaction. This recirculation region contains a pair of vortices with axes in the z direction. The top vortex rotates in the clockwise direction and the bottom vortex rotates in the anticlockwise direction, forming a figure-eight-shaped structure, as observed from the positive z axis.

Further analysis of this vortex pair reveals interesting features. A pair of cone-shaped node structures is formed at the downstream edge of this vortex pair (displayed in Fig. 15). Part of the fluid rotating in the top vortex is captured in the cone-shaped structures. At the tip of these cones, the fluid splits into two streams. One of the streams is ejected in the downstream direction, whereas the other channel is ejected upstream. The channel that is ejected upstream is engulfed by the top vortex. Another ejection mechanism is near the top vortex and is in the lateral direction. This ejected fluid is captured and transported by the axial CVP as it moves past the barrel shock.

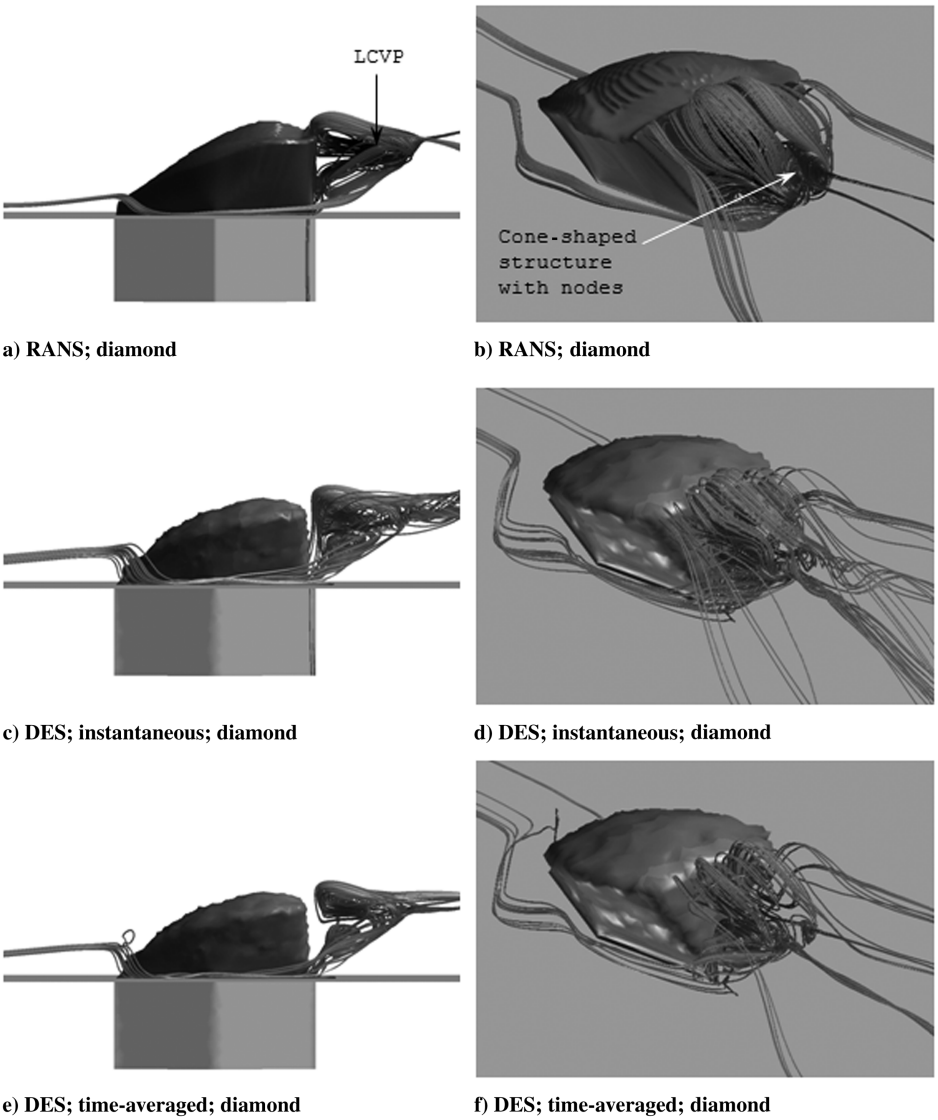

a) RANS; diamond **b) RANS; diamond**

c) DES; instantaneous; diamond **d) DES; instantaneous; diamond**

e) DES; time-averaged; diamond **f) DES; time-averaged; diamond**

Fig. 15 LCVP flow structure observed in the diamond-injector configuration; freestream flow is from left to right for left-column images and from top left to bottom right for right-column images.

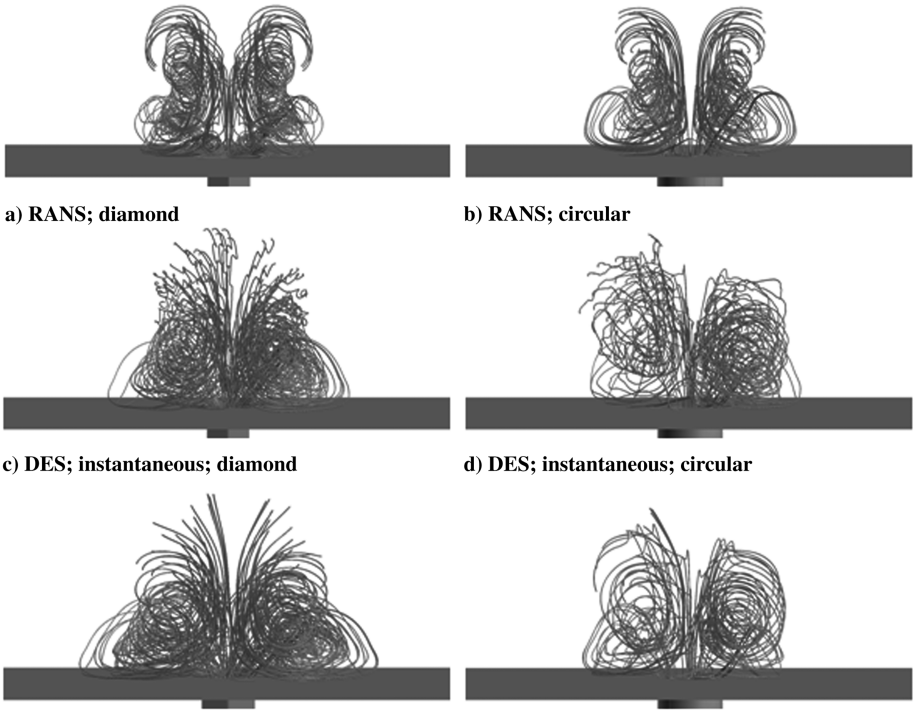

a) RANS; diamond b) RANS; circular

c) DES; instantaneous; diamond d) DES; instantaneous; circular

e) DES; time-averaged; diamond f) DES; time-averaged; circular

Fig. 16 Streamlines showing the axial counter-rotating vortex structures for diamond and circular injectors; freestream flow is exiting out of the page.

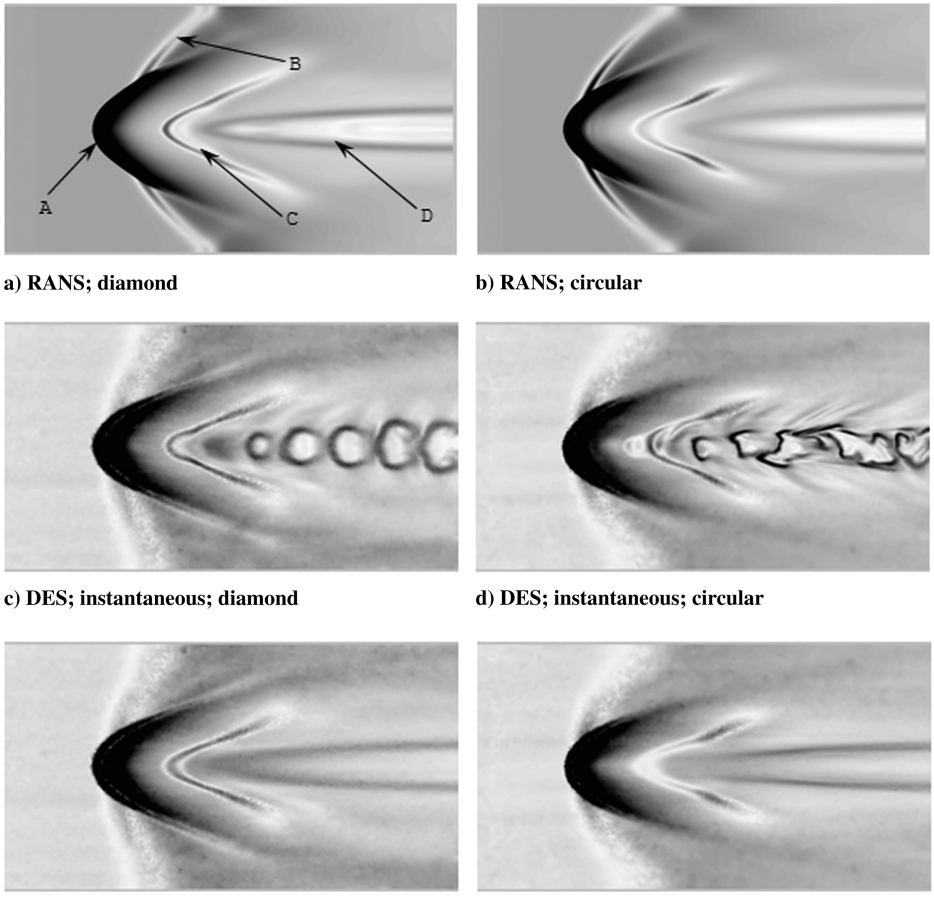

a) RANS; diamond b) RANS; circular

c) DES; instantaneous; diamond d) DES; instantaneous; circular

e) DES; time-averaged; diamond f) DES; time-averaged; circular

Fig. 17 Numerical schlieren showing shock and plume structures on plane $y/d_{\text{eff}} = 2.0$: a) interaction shock, b) lambda shock, c) recompression shock, and d) plume; freestream flow is from left to right.

It is observed that the LCVP entrains fluid from the injector, which enables the vortex pair to act as a potential flame holder in scramjet engines. The advantages of using this structure for flame holding, compared with cavity flame holders, include reduced heat transfer to the wall, because the vortices are not in contact with the tunnel floor and because of the elimination of instabilities induced in the flow due to the presence of cavities [22,23]. Another important requirement for this structure to act as a flame holder is the residence time of the

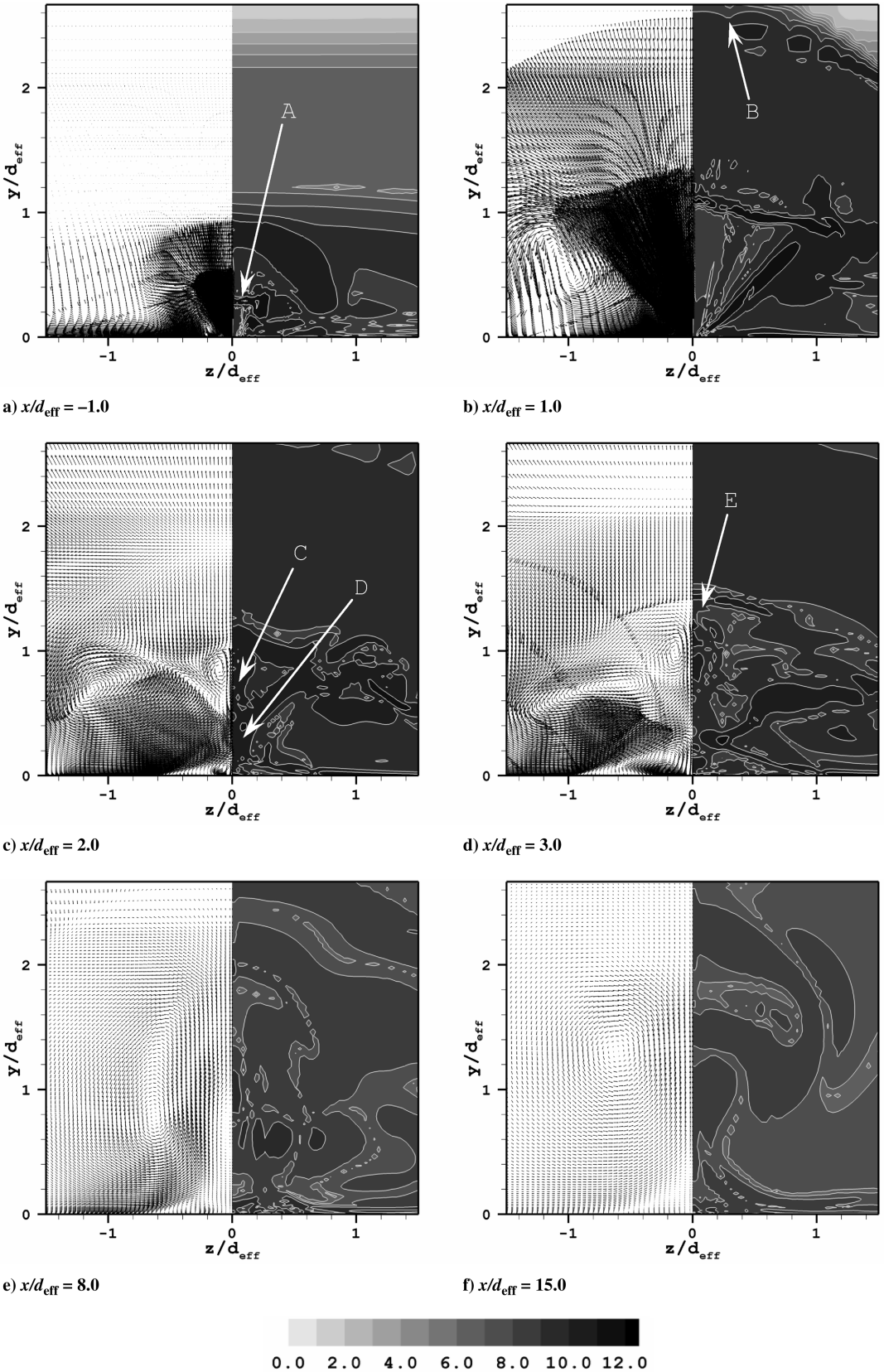

a) $x/d_{\text{eff}} = -1.0$ b) $x/d_{\text{eff}} = 1.0$

c) $x/d_{\text{eff}} = 2.0$ d) $x/d_{\text{eff}} = 3.0$

e) $x/d_{\text{eff}} = 8.0$ f) $x/d_{\text{eff}} = 15.0$

Fig. 18 Compressibility contour plot at various x/d_{eff} locations for y–z velocity vectors (each left half) and contours of compressibility (each right half): a) barrel shock, b) interaction shock, c) cone structure within LCVP, d) wake vortex, and e) recompression shock; contours are plotted in logarithmic scale.

fluid passing through this vortex pair. The average residence time of streamlines passing through this vortex pair is then compared with that of a streamline in the freestream. The streamlines that are trapped in this vortex are in the domain about an order of magnitude longer than the flow. Also, the size of the structure scales with the barrel-shock size and thus the injector-port size. This structure was examined in more detail by Srinivasan and Bowersox [21].

The circular-injector flow structure in this region is different, due to the change in the shape of the barrel shock. The surface of the barrel shock is inclined in the downstream direction. This causes any fluid washed up from the freestream boundary layer to be redirected into the plume; thus, the LCVP was not present.

Axial Counter-Rotating Vortex Pair

The primary mechanism for the mixing of freestream and injector fluid is the CVP. The composition of this vortex pair can be observed in Fig. 16. The interaction between the injector fluid and the freestream boundary layer is the source of the formation of this vortex pair. The leading-edge mixing due to the shear between the injector and freestream fluid is advected downstream. This vorticity gathers additional fluid and eventually forms the axial CVP. The axial ejection mechanism from the nodes of the LCVP pair also contributes to the formation of this vortex pair. Two other sources contribute to the CVP. These are the lateral ejection mechanism from the LCVP and the wake vortex mechanism describe previously. Of all these vortex pairs, only the wake vortices have vorticity opposite to that of the CVP.

Instantaneous Flow Structure

Significant differences in the instantaneous and time-averaged flow structures were observed in the plume/wake region of the flow and the recompression shock. The plume/wake region of the diamond injector is characterized by large-scale structures that are organized. These structures grow in size as the fluid flows downstream from the injector. This can be seen in Figs. 9 and 17. In the case of circular injectors, a lack of organized behavior is apparent. The large-scale structures formed in both test geometries give rise to shock structures that merge with the recompression shock. The circular injector seems to have produced structures that alternate. Approximate estimates of the Strouhal number (approximately 0.2–0.3) indicate that this mechanism was expected.

Vorticity Transport Mechanisms

The data sets obtained from numerical simulations of transverse jet injection into high-speed crossflows were subjected to vorticity transport analysis [24] to estimate the effects of different mechanisms on vortex structures identified in the previous section.

The primitive variable output from the flow solver was processed using the procedure detailed in the Numerical Methods section. The

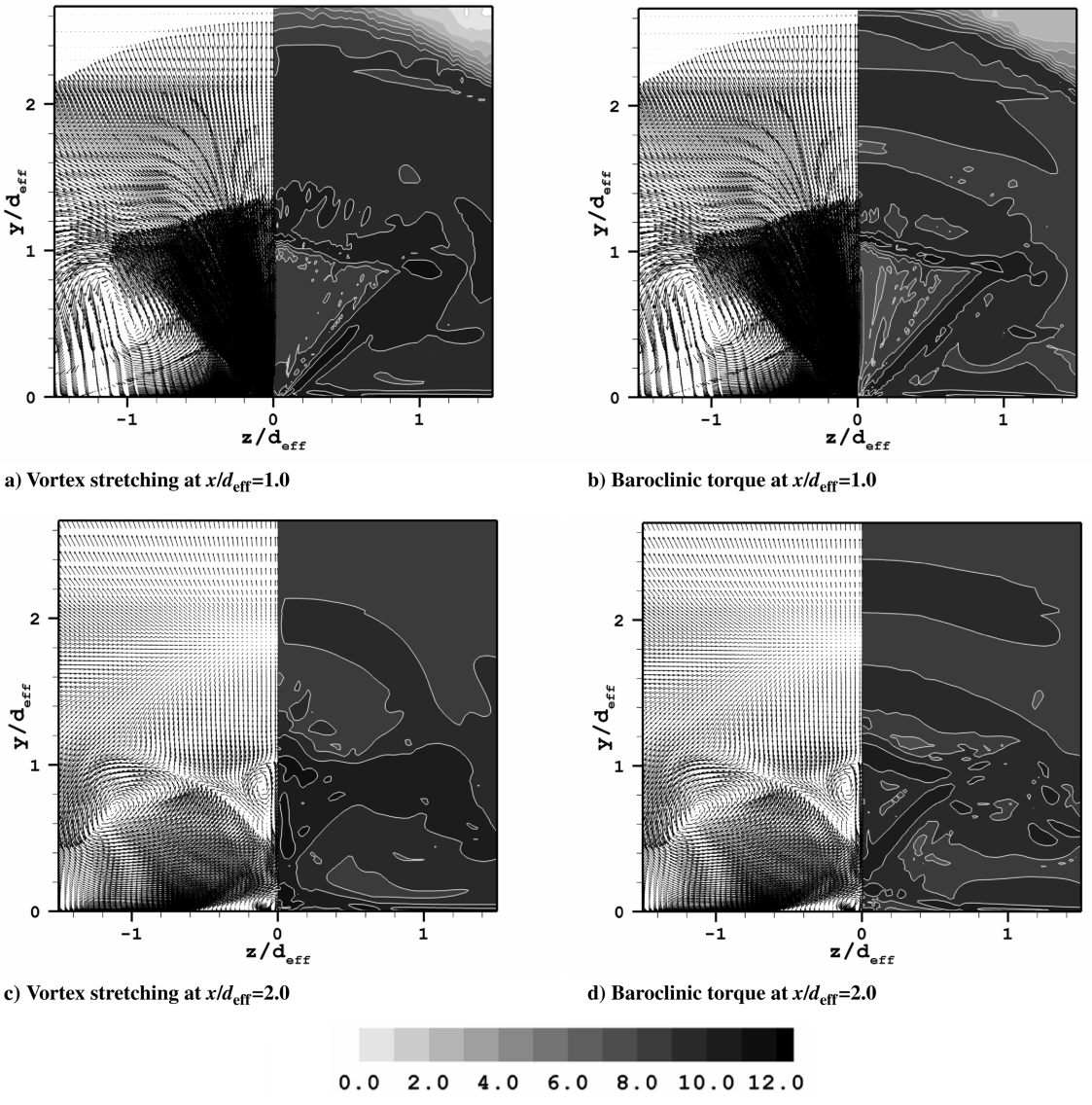

a) Vortex stretching at x/d_{eff}=1.0

b) Baroclinic torque at x/d_{eff}=1.0

c) Vortex stretching at x/d_{eff}=2.0

d) Baroclinic torque at x/d_{eff}=2.0

Fig. 19 Vortex-stretching and baroclinic-torque magnitudes at locations $x/d_{eff} = 1.0$ and 2.0; contours are plotted in logarithmic scale.

terms on the left-hand sides of equations and corresponding y and z equations were recombined into vectors for which the magnitudes were used in this analysis. The results for the compressibility term are shown at six different x/d_{eff} locations. Only those locations that were deemed important are shown for the other terms; a complete listing in given in [25].

Inviscid Terms: Compressibility, Vortex Stretching, and Baroclinic Torque

The magnitude contours of the compressibility term in the vorticity transport equation are plotted in Fig. 18, along with velocity vectors at multiple x/d_{eff} locations. In the plot for the axial location $x/d_{\text{eff}} = -1.0$, the effects of compressibility are apparent around the barrel shock centered on $z/d_{\text{eff}} = 0.0$ and extending to $y/d_{\text{eff}} = +0.25$. The effects of compressibility can also be seen around the interaction shock extending from $z/d_{\text{eff}} = -0.8$ to $+0.8$, with a maximum height of $y/d_{\text{eff}} = +0.9$. At location $x/d_{\text{eff}} = +1.0$, the edges of the barrel shock are indicated by peak values of compressibility. Higher values are also observed in the region around the vortex structure generated by the barrel shock. The outline of the LCVP structure can be observed by noting the peak values at location $x/d_{\text{eff}} = +2.0$. The axial ejection mechanism of the LCVP can be seen at $z/d_{\text{eff}} = 0.0$ and $y/d_{\text{eff}} = +1.0$, along with the corresponding raise in compressibility magnitude. The peak values at this axial location occur near the CVP structure positioned at approximately $z/d_{\text{eff}} = \pm 1.2$ and $y/d_{\text{eff}} = +0.7$. From the images shown for the compressibility, it is apparent that the largest magnitudes occur at locations $x/d_{\text{eff}} = +1.0$ and $+2.0$. Therefore, only these planes are displayed for the remaining terms in the vorticity transport equation.

The axial planes for the vortex-stretching (left images) and baroclinic terms (right images) are shown in Fig. 19. The contours at location $x/d_{\text{eff}} = +1.0$ show the effects of vortex stretching around the lateral edge of the barrel shock. The predominant areas of vortex stretching can be seen at location $x/d_{\text{eff}} = +2.0$. The axial ejection mechanism of the LCVP pushing fluid downstream and upstream with the cone-shaped nodes contributes to the large magnitudes of vortex stretching. The lateral ejection and merging of the LCVP fluid with the CVP can also be observed. The stretching of the wake vortex is seen around $z/d_{\text{eff}} = 0.0$ and $y/d_{\text{eff}} = 0.0$. It was noted that the wake vortex has the highest vortex-stretching values at $x/d_{\text{eff}} = +3.0$. The high vortex-stretching values persist as the wake vortices lift off the floor and begin to merge with the CVP.

The physical effects of compressibility and vortex stretching are contradictory. The compressibility or dilatational term tends to expand a given region of fluid, whereas the effect of vortex stretching is to reduce the volume. Thus, the interaction of these two terms has considerable bearing on the evolution of the vorticity in the flowfield.

Baroclinic torque is generated by the misalignment of the density and pressure gradient vectors. The magnitude of the baroclinic-torque vector at two different axial locations is plotted in Fig. 19. The misalignment of the density and pressure gradient vectors around the barrel and the interaction shocks can be seen in the contours at

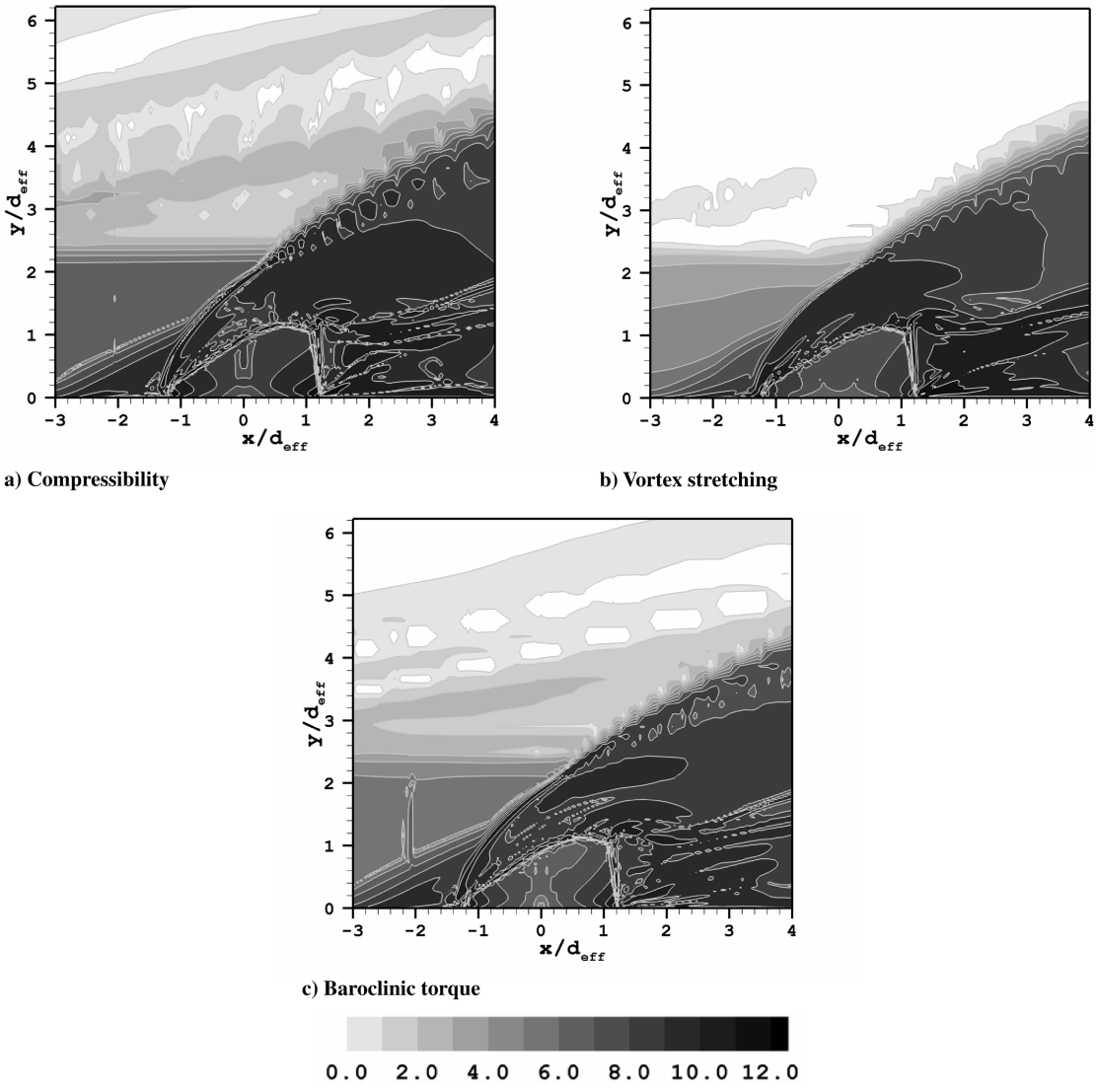

a) Compressibility

b) Vortex stretching

c) Baroclinic torque

Fig. 20 Magnitude of inviscid terms on the right-hand side of the vorticity transport equation; contours are plotted in logarithmic scale.

location $x/d_{\text{eff}} = +1.0$. The interaction shock peak is at location $y/d_{\text{eff}} = +2.6$ and is represented by contours that indicate that the baroclinic-torque magnitude is approximately an order of magnitude smaller than that at the barrel shock. Large magnitudes are observed near the core of the initial leading-edge mixing vortex. At $x/d_{\text{eff}} = +2.0$, the peak values around the CVP vortex near the periphery of the plotted domain are lower by an order of magnitude than with the magnitudes of compressibility and vortex stretching. This is also the trend within the LCVP structure, in which the baroclinic-torque magnitude is about two orders of magnitude lower than vortex stretching. The recompression shock can also be seen at location $y/d_{\text{eff}} = +1.6$. There is little effect of this torque at downstream locations.

A plot of the compressibility, vortex stretching, and baroclinic-torque contours around the injector in the x–y plane is shown in Fig. 20. In the region just downstream of the barrel shock, it was observed that compressibility and vortex-stretching terms dominate over the effects of the baroclinic torque. As discussed before, the axial and lateral ejection mechanisms within the LCVP contribute to the large magnitudes of the vortex-stretching term.

Viscous Terms: Laminar and Turbulent Diffusion

The laminar and turbulent diffusion magnitudes and their anisosteric counterparts are plotted in Figs. 21 and 22. The initial plots around the injector leading and trailing edges are significantly different for the laminar and turbulent contours. The turbulent diffusion magnitude is approximately four orders of magnitude higher than the laminar diffusion in the entire region between the barrel shock and the interaction shock. This is possibly due the shear interaction between the injector and freestream fluids. Higher turbulent diffusion values are also observed near the top surface of the barrel shock at $x/d_{\text{eff}} = +1.0$. Downstream of this location, the relative values of the laminar and turbulent terms are more comparable, with the turbulent terms being an order of magnitude higher. The peak values observed in both cases generally coincide with the vortex cores that constitute the CVP. The anisosteric laminar and turbulent terms show that their effect on the vorticity production is relatively low, compared with the other terms in the transport equation, especially the inviscid terms.

Vorticity Components vs Production and Transport

Following the example of Lee et al. [26], the individual components of vorticity were integrated over several cross-sectional planes of the domain and the results are plotted in Fig. 23. The center of the injector is indicated by a vertical line in the plot. It was found that the x and y components of vorticity were essentially zero up to the leading edge of the injector, whereas the z component was nonzero due to vorticity present in the freestream boundary layer. At the leading edge of the injector, there was an increase in the x vorticity, followed by an increase in the y component downstream of

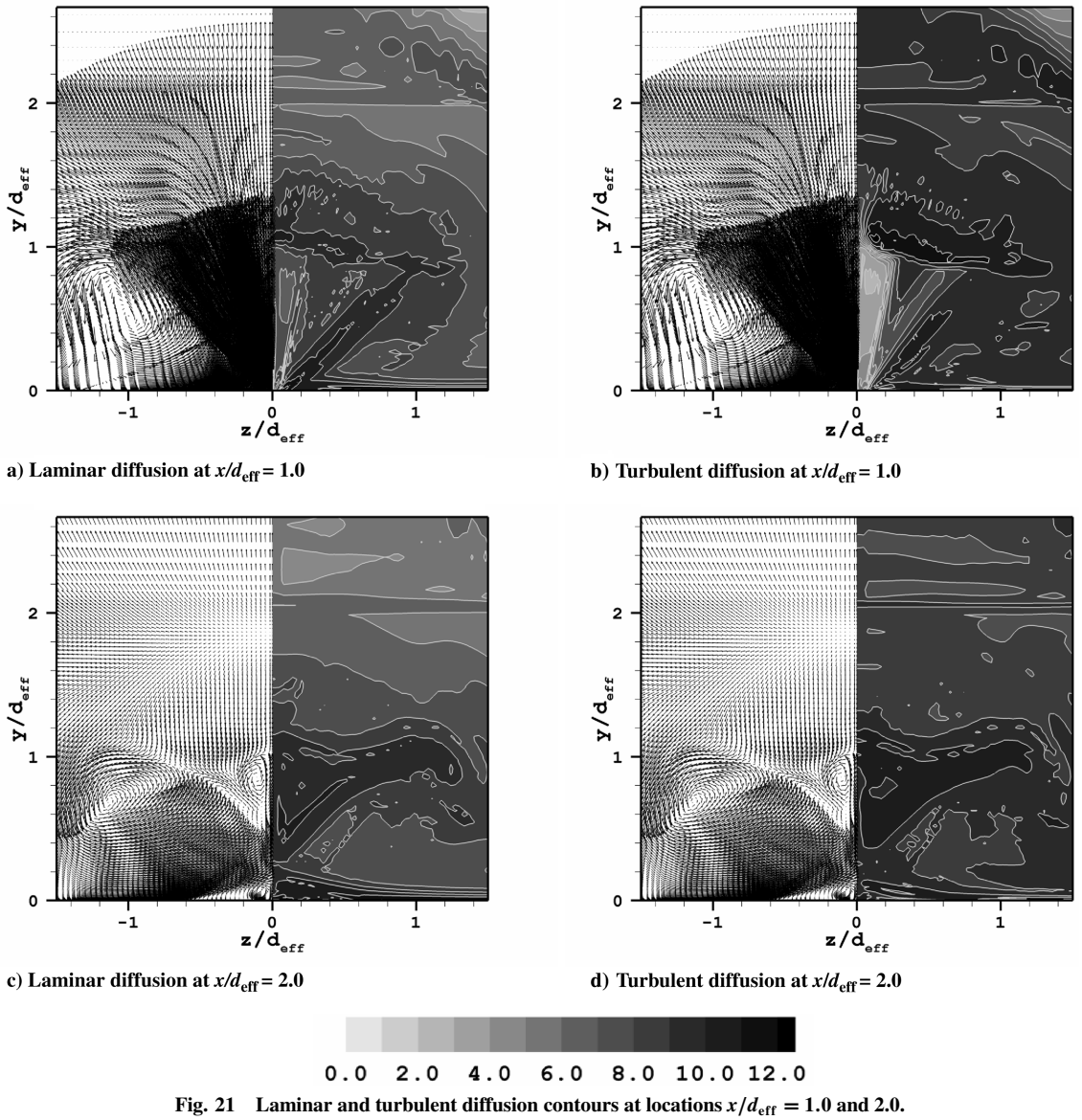

a) Laminar diffusion at $x/d_{\text{eff}} = 1.0$

b) Turbulent diffusion at $x/d_{\text{eff}} = 1.0$

c) Laminar diffusion at $x/d_{\text{eff}} = 2.0$

d) Turbulent diffusion at $x/d_{\text{eff}} = 2.0$

Fig. 21 Laminar and turbulent diffusion contours at locations $x/d_{\text{eff}} = 1.0$ and 2.0.

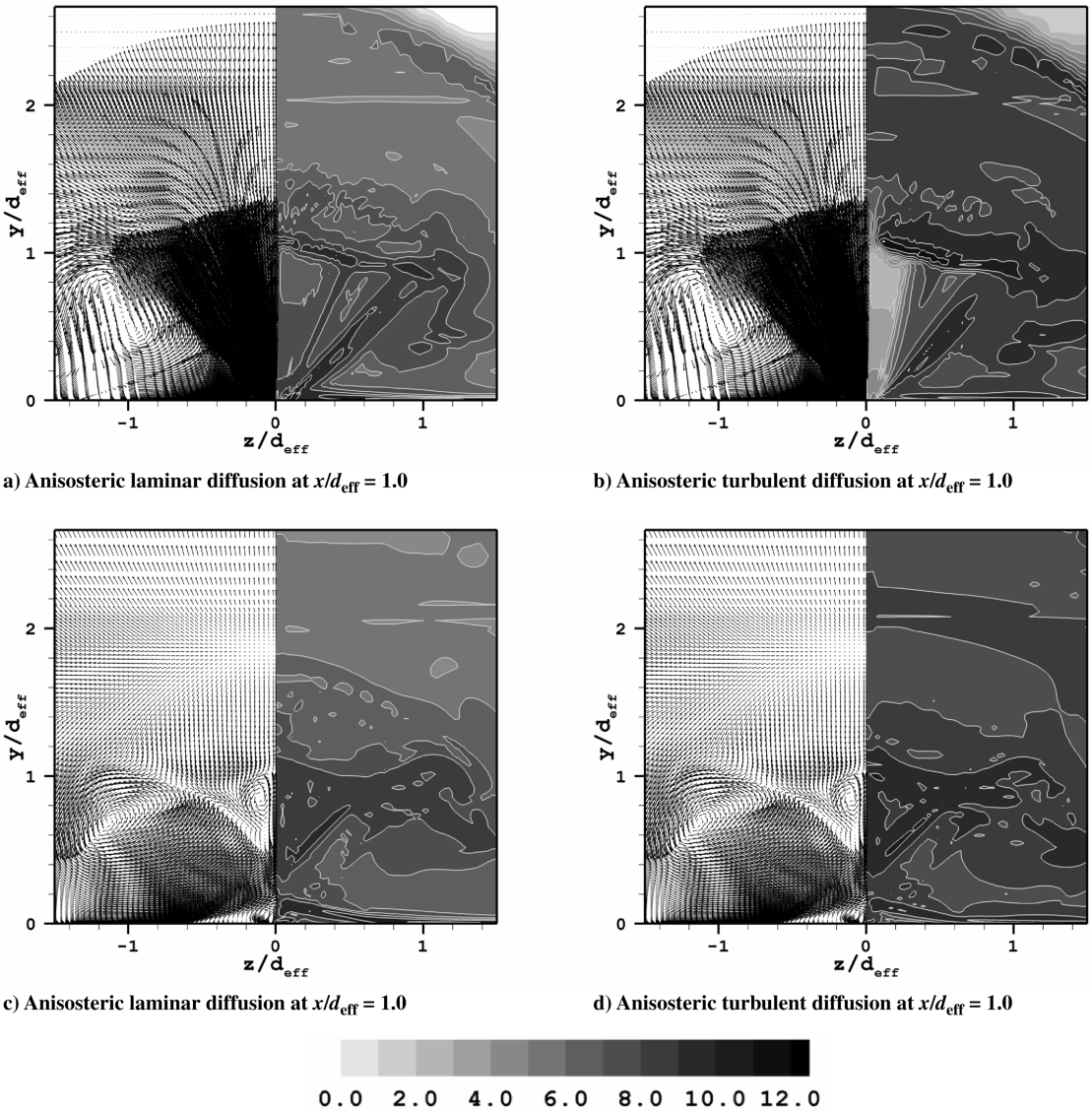

a) Anisosteric laminar diffusion at $x/d_{\text{eff}} = 1.0$

b) Anisosteric turbulent diffusion at $x/d_{\text{eff}} = 1.0$

c) Anisosteric laminar diffusion at $x/d_{\text{eff}} = 1.0$

d) Anisosteric turbulent diffusion at $x/d_{\text{eff}} = 1.0$

Fig. 22 Anisosteric laminar and turbulent diffusion contours at locations $x/d_{\text{eff}} = 1.0$ and 2.0.

the leading edge of the injector. It was noted that the x-vorticity plot across the injector corresponds to the formation of the leading-edge vortices. An abrupt reduction in x vorticity is seen at the trailing edge of the injector in which the barrel shock terminates. The increase in the y-vorticity levels is higher than in the x-vorticity levels. The large increase in z vorticity near the trailing edge is due to the flow structures associated with LCVP. At 4^*d_{eff} downstream of the injector, the z vorticity reduces to the original freestream values.

A line plot for the right-hand side terms in the compressible vorticity transport equation is also shown in Fig. 23. All the terms in the plot show peak values around the trailing edge of the injector, following the trend of the vorticity plots. The largest increase (about four orders of magnitude) is seen in the vortex-stretching term, which also has the highest peak value of any other term except laminar diffusion. The peak values of compressibility coincide with those of vortex stretching. A steep rise in the baroclinic term is also seen, but the peak value is lower than with the first two terms. Of the first three terms, it was noted that the increase in vortex stretching persists over a longer time within the domain. The laminar diffusion term has the highest overall value, but it is confined to the boundary layer. This is also seen in the contour plots discussed previously. The turbulent diffusion term increases at the leading edge of the injector and has a local minima at the injector trailing edge, after which it has a peak at the LCVP location. Finally, both the anisosteric laminar and diffusion terms follow similar trends, peaking at the LCVP location and gradually returning to their freestream values at the end of the domain.

Conclusions

Numerical simulations were performed to study the flowfields generated by transverse sonic injection through diamond and circular injectors into a Mach 5.0 freestream flow. The simulations were performed using RANS and DES turbulence models. Apart from providing a high-resolution result of the flowfield, the DES model provided a basis for the evaluation of the performance of the RANS model in predicting this flowfield. All of the numerical results were compared against available experimental data, and the performance of the models was found to be adequate. A detailed characterization of the shock and vortex structures in the flow was performed for both diamond- and circular-shaped injectors. For the diamond part, two new vortex structures were identified. The leading-edge mixing mechanism was prominent in the diamond-injector case and has the benefit of increasing fuel–air mixing. The circular injector also generated a leading-edge mixing mechanism with a different configuration. The lateral counter-rotating vortex pair was observed only in the diamond-injector configuration and has the potential to act as a gas-dynamic flame holder [21]. These new structures were observed in both RANS and DES simulations (time-averaged and instantaneous). Large-scale structures were observed in the plume/

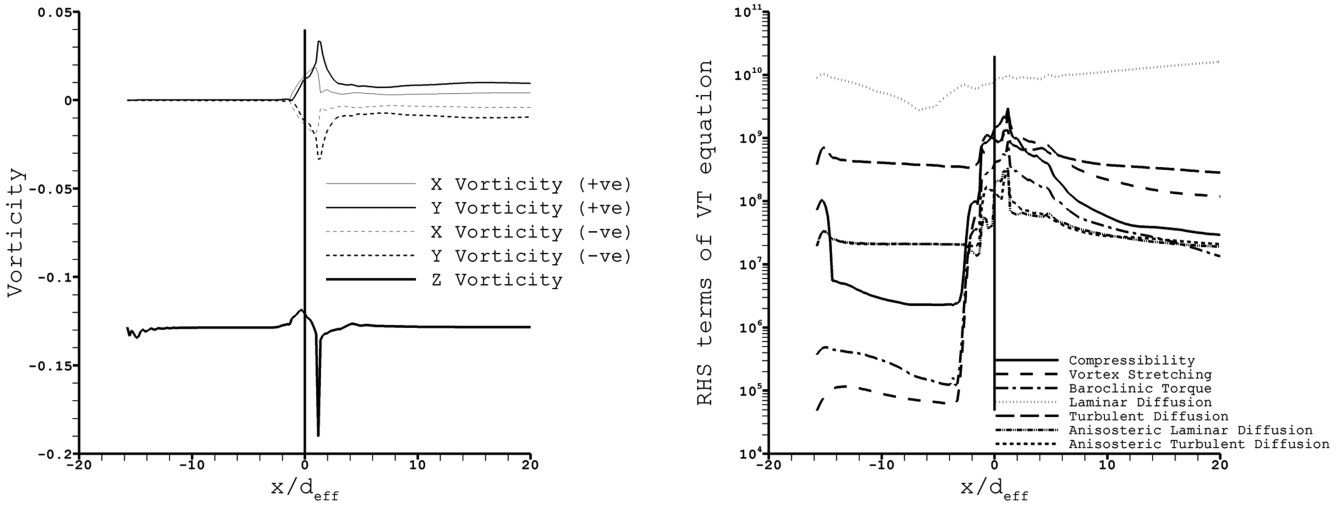

a) Vorticity components along the axial direction **b) VT terms along the axial direction**

Fig. 23 Magnitudes of vorticity and transport terms in the right-hand side of the VT equation.

wake region of the flowfield for both injector geometries. These structures were more organized in the diamond-injector test case. Comparing the RANS and time-averaged DES results, it was found that the prediction capabilities of RANS are adequate for these flowfields. The compressible vorticity transport equation was solved for the magnitudes of the inviscid and viscous terms. An in-house program was used to analyze the diamond-injector structured-grid RANS solution. The inviscid quantities of compressibility, vortex stretching, and baroclinic torque were found to be predominant in important regions of the flowfield. In the LCVP region downstream of the barrel shock, the effect of the baroclinic term was found to be diminished, compared with the other two inviscid terms. Planar-averaged results for the transport quantities confirmed this behavior. High values of vortex stretching were observed in the wake vortices. Vortex stretching was found to persist longer than the other terms.

References

[1] Beach, H. L., and Blankson, I. M., Jr., "Prospects for Future Hypersonic Air-Breathing Vehicles," International Aerospace Planes Conference, Orlando, FL, AIAA Paper 1991-5009, 1991.

[2] Chenault, L., Beran, P., and Bowersox, R., "Numerical Investigation of Supersonic Injection Using a Reynolds-Stress Turbulence Model," *AIAA Journal*, Vol. 37, No. 10, 1999, pp. 1257–1269.

[3] Billig, F. S., and Schetz, J. A., "Penetration of Gaseous Jets Injected into a Supersonic Stream," *Journal of Spacecraft and Rockets*, Vol. 35, No. 11, 1966, pp. 1658–1665.

[4] Spaid, F. W., and Zukowski, E. E., "Secondary Injection of Gases into a Supersonic Flow," *AIAA Journal*, Vol. 2, No. 10, 1964, pp. 1689–1696.

[5] Heiser, W., and Pratt, D., *Hypersonic Airbreathing Propulsion*, 1st ed., AIAA Education Series, AIAA, Washington, D.C., 1994.

[6] Weber, R., and McKay, J., "Analysis of Ramjet Engines Using Supersonic Combustion," NACA Lewis Flight Propulsion Lab. TN 4386, Cleveland, OH, Sept. 1958.

[7] Tomioka, S., Jacobsen, L., and Schetz, J., "Sonic Injection from Diamond-Shaped Orifices into a Supersonic Flow," *Journal of Propulsion and Power*, Vol. 19, No. 1, 2003, pp. 104–114.

[8] Barber, M. J., Schetz, J. A., and Roe, L. A., "Normal, Sonic Helium Injection Thorough a Wedge Shaped Orifice into a Supersonic Flow," *Journal of Propulsion and Power*, Vol. 13, No. 2, 1997, pp. 257–263.

[9] Bowersox, R., Fan, H., and Lee, D., "Sonic Injection into a Mach 5.0 Freestream Through Diamond Orifices," *Journal of Propulsion and Power*, Vol. 20, No. 2, 2004, pp. 280–287. doi:10.2514/1.9254

[10] GASP, Software Package, Ver. 4.0, AeroSoft, Inc., Blacksburg, VA, 2001.

[11] Wilcox, D. C., "Reassessment of the Scale-Determining Equation for Advanced Turbulence Models," *AIAA Journal*, Vol. 26, No. 11, 1988, pp. 1299–1310.

[12] Neel, R. E., Godfrey, A. G., and Slack, D. C., "Turbulence Model Validation in GASP Ver. 4," 33rd AIAA Fluid Dynamics Conference and Exhibit, Orlando, FL, AIAA Paper 2003-3740, 2003.

[13] Roe, P. L., "Approximate Riemann Solvers, Parameter Vector, and Difference Schemes," *Journal of Computational Physics*, Vol. 43, No. 2, 1981, pp. 357–372. doi:10.1016/0021-9991(81)90128-5

[14] Harten, A., "High Resolution Schemes for Hyperbolic Conservation Laws," *Journal of Computational Physics*, Vol. 49, No. 3, Mar. 1983, pp. 357–393. doi:10.1016/0021-9991(83)90136-5

[15] Hirsch, C., *Numerical Computation of Internal and External Flows*, 1st ed., Vol. 1–2, Wiley, New York, 1988.

[16] Wilcox, D. C., *Turbulence Modeling for CFD*, 2nd ed., DCW Industries, Inc., La Canada, CA, 1998.

[17] Strang, W. Z., Tomaro, R. F., and Grismer M. J., "The Defining Methods of Cobalt 60: A Parallel, Implicit, Unstructured Euler/Navier–Stokes Flow Solver," 37th Aerospace Sciences Meeting and Exhibit, Reno, NV, AIAA Paper 1999-786, 1999.

[18] Gottlieb, J. J., and Groth, C. P. T., "Assessment of Riemann Solvers for Unsteady One-Dimensional Inviscid Flows for Perfect Gases," *Journal of Computational Physics*, Vol. 78, No. 2, Oct. 1988, pp. 437–458. doi:10.1016/0021-9991(88)90059-9

[19] Strelets, M., "Detached Eddy Simulation of Massively Separated Flow," 39th Aerospace Sciences Meeting and Exhibit, Reno, NV, AIAA Paper 2001-879, 2001.

[20] Gruber, M. R., Nejad, A. S., Chen, T. H., and Dutton, J. C., "Transverse Injection from Circular and Elliptic Nozzles into a Supersonic Crossflow," *Journal of Propulsion and Power*, Vol. 16, No. 3, 2000, pp. 449–457.

[21] Srinivasan, R., and Bowersox, R., "Simulation of Transverse Gaseous Injection Through a Diamond Port into a Supersonic Freestream," *Journal of Propulsion and Power*, Vol. 23, No. 4, 2007, pp. 772–782. doi:10.2514/1.18405

[22] Davis, D. L., and Bowersox, R. D. W., "Stirred Reactor Analysis of Cavity Flame Holders for Scramjets," 33rd AIAA/ASME/SAE/ASEE Joint Propulsion Conference and Exhibit, Seattle, WA, AIAA Paper 1997-3274, 1997.

[23] Davis, D. L., and Bowersox, R. D. W., "Computational Fluid Dynamics Analysis of Cavity Flame Holders for Scramjets," 33rd AIAA/ASME/SAE/ASEE Joint Propulsion Conference and Exhibit, Seattle, WA, AIAA Paper 1997-3270, 1997.

[24] Bowersox, R., "Turbulent Flow Structure Characterization of Angled Injection into a Supersonic Crossflow," *Journal of Spacecraft and Rockets*, Vol. 34, No. 2, 1996, pp. 205–213.

[25] Srinivasan, R., "Improved Understanding and Control of High-Speed Jet Interaction Flows," Ph.D. Dissertation, Aerospace Engineering, Texas A&M University, College Station, TX, 2005.

[26] Lee, S. H., Kim, Y. J., and Mitani, T., "Mixing Augmentation of Transverse Injection in Scramjet Combustor," 38th Aerospace Sciences Meeting and Exhibit, Reno, NV, AIAA Paper 2000-0090, 2000.

T. Jackson
Associate Editor